



# CHALMERS

## **NOVEL POWERTRAIN TOPOLOGIES FOR ENERGY-EFFICIENT BATTERY ELECTRIC VEHICLES**

YU XU

---

Division of Energy Conversion and Propulsion Systems  
Department of Mechanics and Maritime Sciences  
CHALMERS UNIVERSITY OF TECHNOLOGY  
Göteborg, Sweden 2023



THESIS FOR THE DEGREE OF LICENTIATE OF ENGINEERING IN THERMO  
AND FLUID DYNAMICS

NOVEL POWERTRAIN TOPOLOGIES FOR  
ENERGY-EFFICIENT BATTERY ELECTRIC VEHICLES

YU XU

Department of Mechanics and Maritime Sciences  
CHALMERS UNIVERSITY OF TECHNOLOGY

Göteborg, Sweden 2023

NOVEL POWERTRAIN TOPOLOGIES FOR ENERGY-EFFICIENT BATTERY  
ELECTRIC VEHICLES  
YU XU

© YU XU, 2023

Thesis for the degree of Licentiate of Engineering 2023:15  
Division of Energy Conversion and Propulsion Systems  
Department of Mechanics and Maritime Sciences  
Chalmers University of Technology  
SE-412 96 Göteborg  
Sweden  
Telephone: +46 (0)72-574 31 08

Chalmers Reproservice  
Göteborg, Sweden 2023

# ABSTRACT

The global transition towards sustainable transportation has underscored the importance of battery electric vehicles (BEVs), with a growing need for enhancement in powertrain energy efficiency to mitigate range anxiety and promote widespread adoption. In response to this need, there have been significant contributions from advancements on powertrain components, such as electric motors and inverters, towards increased energy efficiency. However, it is crucial to acknowledge that BEV powertrain efficiency is not simply a product of the efficiencies of electric motors and inverters. In this context, the exploration of novel powertrain topologies presents itself as an alternative and promising approach for further enhancing BEV powertrain efficiency. Moreover, when component-level advancements are integrated with innovative powertrain topologies, there is potential to push the boundaries of powertrain energy efficiency in BEVs.

To this end, system simulation techniques are utilized in this thesis to evaluate different powertrain topologies in terms of energy efficiency over standard drive cycles, each operating under its optimal powertrain strategy. Specifically, two powertrain topologies are investigated in this thesis: 1) the Adaptive Front- and Rear-Axle Independently Driven (AFRID) powertrain features two clutches that enable the mechanical disconnection of two electric motors with differentiated high-efficiency operating areas, aiming to address the inherent high no-load losses of dual motor powertrains while utilizing the high-efficiency zone of each motor and leveraging torque distribution functionality to enhance overall efficiency. 2) The adjustable DC-link voltage powertrain allows the adjustment of DC-link voltage to an efficiency-favored level irrespective of the battery voltage, in response to dynamically changing driving conditions.

The findings of this thesis indicate that the integration of both investigated powertrain topologies with state-of-the-art components can significantly enhance powertrain energy efficiency in comparison to conventional BEV powertrains. Importantly, these improvements in efficiency do not come at the expense of vehicle performance or driveability; in fact, vehicles equipped with these novel powertrain topologies are observed to exhibit superior performance and improved driveability, making them highly favorable options for the next generation of BEV powertrains.

**Keywords:** Battery electric vehicle, Electric powertrain, Energy efficiency, Powertrain topologies, System simulation, Vehicle performance



## LIST OF PUBLICATIONS

This thesis is based on the work contained in the following publications:

**Publication I** Y. Xu, A. Kersten, S. Klacar, B. Ban, J. Hellsing, and D. Sedarsky. "Improved efficiency with adaptive front and rear axle independently driven powertrain and disconnect functionality."

*Transportation Engineering, Volume 13, Pages 100192, 2023*

**Publication II** Y. Xu, A. Kersten, S. Klacar, and D. Sedarsky. "Maximizing Efficiency in Smart Adjustable DC Link Powertrains with IGBTs and SiC MOSFETs via Optimized DC-Link Voltage Control."

*Batteries, Volume 9, Number 6, Pages 302, 2023*





## ACKNOWLEDGEMENTS

The research work presented in this thesis has been funded by China Euro Vehicle Technology AB and Energimyndigheten, without which this project would not have been feasible.

I would like to thank my academic supervisor, Prof. David Sedarsky, for your trust in me and the freedom you granted in my research work. Your unwavering support and encouragement, particularly when I approached you with crazy ideas and thoughts, have been immensely valuable.

I am deeply grateful to my industrial supervisor Dr. Simon Klacar for your exceptional guidance both in the technical area and in broader life lessons through all these years, which has not only shaped my professional path but also a foundational pillar in my personal growth and development. With a rich industry experience, particularly in the powertrain system, and insightful perspectives, you have continually inspired me. Your constructive feedback on my writings and our discussion has always been a beacon. Beyond the technical aspects, your steadfast support and encouragement on every step of my journey have been indispensable.

My appreciation extends to Johan Hellsing, who initiated the project and played a pivotal supervisory role during the CEVT time. Our technical discussions have enriched my learning immensely. Further, I am deeply thankful to Dr. Anton Kersten for being an outstanding colleague and friend. Your expert guidance on academic writing combined with profound insights into power electronics have been invaluable to my work. Your encouragement and cheer have consistently energized me to continue the demanding journey in the academic world.

A heartfelt acknowledgment is extended to Dr. Pär Ingelstöröm, Dr. Andreas Andersson, Shino George, and Dr. Jianning Zhao, as well as all the technical support from Infimotion. Your collective expertise and advice on electric drive systems have been a cornerstone of my research.

I am also thankful to my project coordinator John Bergström, my managers Matthias Abrahamsson and Mark Saukkonen for your invaluable support and efficiently sorting out all the administrative complexities, facilitating my focus on the research itself.

Furthermore, I extend my gratitude to my colleagues at the Chalmers ECAPS division and to those at CEVT electric drive, system simulation and energy dynamics teams. Your selfless sharing of knowledge and advice has been invaluable to my work.

And, most importantly, I could not have achieved all of this without the unconditional support, love, and belief from my girlfriend, Ann-Sofie Eriksson. Sincerely, your presence has been the backbone of this journey, shouldering countless hours and days with resilience and strength, ensuring I was never alone in this endeavor. Every step was imbued with courage, knowing you were with me all along.

Yu

Gothenburg  
October 2023.

# Contents

<b>Abstract</b>	<b>i</b>
<b>List of publications</b>	<b>iii</b>
<b>Acknowledgements</b>	<b>v</b>
<b>List of Figures</b>	<b>ix</b>
<b>List of Tables</b>	<b>xi</b>
<b>1 Introduction</b>	<b>1</b>
1.1 Motivation . . . . .	1
1.2 Electric powertrain energy efficiency . . . . .	2
1.3 Related works . . . . .	3
1.3.1 Component-level optimization . . . . .	3
1.3.2 System-level approach . . . . .	4
1.4 Objectives . . . . .	5
<b>2 Background</b>	<b>7</b>
2.1 Drive cycles . . . . .	7
2.2 Powertrain system simulation . . . . .	7
2.3 Powertrain energy management strategy . . . . .	9
2.3.1 Heuristic strategy . . . . .	9
2.3.2 Dynamic programming . . . . .	9
<b>3 Modeling</b>	<b>13</b>
3.1 Longitudinal vehicle dynamics . . . . .	13
3.2 Battery . . . . .	15
3.3 Electric motor . . . . .	16
3.4 Converters . . . . .	18
3.4.1 DC-DC converter . . . . .	19
3.4.2 DC-AC inverter . . . . .	20
3.5 Transmission . . . . .	21
<b>4 Adaptive Front and Rear Axle Independently Driven Powertrain</b>	<b>23</b>

4.1	Powertrain configuration . . . . .	23
4.2	Powertrain controller . . . . .	25
4.2.1	Supervisory controller . . . . .	25
4.2.2	EDU speed controller . . . . .	27
4.3	Powertrain operation strategy . . . . .	28
4.3.1	Optimal torque distribution strategy in AWD mode . . . . .	29
4.3.2	Powertrain mode selection strategy . . . . .	30
4.4	Simulation setup . . . . .	33
4.5	Results and discussion . . . . .	33
4.5.1	Transient energy loss . . . . .	33
4.5.2	Effect of mode selection strategy . . . . .	34
4.5.3	Energy efficiency improvement . . . . .	36
<b>5</b>	<b>Adjustable DC-Link Voltage Powertrain</b>	<b>37</b>
5.1	Powertrain configuration . . . . .	39
5.2	Powertrain operation strategy . . . . .	39
5.2.1	DC-link voltage operating boundary . . . . .	40
5.2.2	DC-link voltage selection strategy . . . . .	40
5.3	Simulation setup . . . . .	42
5.4	Results and discussion . . . . .	42
5.4.1	Optimized DC-link voltage . . . . .	43
5.4.2	Energy efficiency improvement . . . . .	44
5.4.3	Vehicle performance improvement . . . . .	45
<b>6</b>	<b>Conclusion and Future Work</b>	<b>49</b>
6.1	Conclusion and Discussion . . . . .	49
6.2	Future work . . . . .	51
	<b>Bibliography</b>	<b>53</b>

# List of Figures

1.1	Electric car registrations and sales share in China, United States and Europe, 2018-2022. [5]	1
1.2	Conventional BEV powertrain structure.	2
1.3	Sankey diagram of a conventional BEV powertrain under a specific drive cycle.	3
1.4	The component level and system level approaches to improve BEV powertrain energy efficiency with examples. [34–36]	5
2.1	WLTC vehicle speed profile.	7
2.2	Information flow of backward simulation. [42]	8
2.3	Information flow of forward simulation. [42]	8
3.1	Illustration of forces acting on vehicle longitudinal direction.	13
3.2	Battery equivalent circuit model.	15
3.3	Battery (pack level) data tested under charge and discharge conditions: (a) open circuit voltage and (b) internal resistance.	15
3.4	Electric motor types with “Suitable for vehicle propulsion” highlighted by AVL. [55]	16
3.5	PMSM equivalent electric circuit model.	17
3.6	Current density distributions in copper windings at high frequency operation. [9]	18
3.7	Bidirectional boost DC-DC converter: (a) with IGBTs and (b) with MOSFETs.	19
3.8	Three-phase inverter: (a) with IGBTs and (b) with MOSFETs.	21
4.1	AFRID powertrain structure.	24
4.2	Structure of dog clutch assembly.	24
4.3	EDU efficiency map: (a) front, (b) rear and (c) corresponding efficiency difference map.	25
4.4	AFRID powertrain supervisory controller scheme.	26
4.5	Dog clutch engagement processes.	27
4.6	The scheme of energy-efficient EDU speed control process.	28
4.7	Energy-efficient EDU speed control torque trajectories to be followed when accelerating or decelerating the EDU.	29
4.8	Optimal torque distribution ratio $\alpha_{\text{opt}}$ in AWD mode.	30
4.9	Powertrain losses at different modes: (a) FWD, (b) RWD and (c) AWD.	31
4.10	Minimum powertrain loss and corresponding operating mode.	32
4.11	EDU transient energy loss during the speed control process.	32

4.12	GT-Suite model architecture. . . . .	33
4.13	Instantaneous powertrain power losses of FRID powertrain and AFRID powertrain with rule-based mode selection strategy. . . . .	34
4.14	Operating modes derived from rule-based and DP-based selection strategies for the AFRID powertrain under the WLTC drive cycle. . . . .	35
4.15	Instantaneous powertrain power losses of AFRID with DP- and rule-based mode selection strategy during the WLTC drive cycle between 1536 s and 1548 s. . . . .	36
5.1	Illustration of maximum-torque-per-ampere (MTPA) control strategy. . .	37
5.2	PMSM loss maps: (a) with 250 V DC voltage and (b) with 450 V DC voltage. .	38
5.3	Inverter loss maps (Infineon FS820R08A6P2B): (a) with 250 V DC voltage and (b) with 450 V DC voltage. . . . .	38
5.4	Adjustable DC-link voltage powertrain configuration with bidirectional DC-DC converter. . . . .	39
5.5	Schematic illustration of the inverter/PMSM and DC-DC converter control for the adjustable DC-link voltage powertrain. . . . .	42
5.6	Optimized DC-link voltage in adjustable DC-link voltage powertrain compared with DC-link voltage in baseline powertrain: (a) IGBT-based powertrains with low battery SoC, (b) MOSFET-based powertrains with low battery SoC, (c) IGBT-based powertrains with high battery SoC and (d) MOSFET-based powertrains with high battery SoC. . . . .	43
5.7	Powertrain losses breakdown under WLTC drive cycle: (a) low battery SoC and (b) high battery SoC. . . . .	46
5.8	Results of 0 - 100 km/h acceleration: (a) DC-link voltage and (b) motor torque output. . . . .	47
6.1	Comparison of energy consumption for different drive cycles and different system voltages: (a) passenger car and (b) heavy-duty truck. [88] . . . .	50

# List of Tables

3.1	Main vehicle parameters. . . . .	14
4.1	WLTC energy consumption of current BEV models with FRID powertrains and single motor powertrain. [79] . . . . .	23
4.2	EDU and clutch engagement states for each operating mode. . . . .	24
4.3	Description of energy-efficient EDU speed control torque derivation. . . .	28
4.4	Comparison of max/min torque and energy-efficient EDU speed control. . . .	34
4.5	Comparison of rule-based and DP mode selection strategy. . . . .	35
4.6	Energy consumption of FRID, AFRID and single motor powertrain under WLTC drive cycle. . . . .	36
5.1	Energy consumption of baseline and adjustable DC-link voltage powertrain under WLTC drive cycle. . . . .	44
5.2	0 - 100 km/h acceleration time simulation results. . . . .	46
6.1	Coefficients of polynomial equations for solving battery current. . . . .	61





# Nomenclature

## Abbreviations

AC	<b>A</b> lternating <b>C</b> urrent
AWD	<b>A</b> ll- <b>W</b> heel- <b>D</b> rive
BEV	<b>B</b> attery <b>E</b> lectric <b>V</b> ehicle
CVT	<b>C</b> ontinuous <b>V</b> ariable <b>T</b> ransmission
DC	<b>D</b> irect <b>C</b> urrent
DMTS	<b>D</b> ual- <b>m</b> otor <b>T</b> wo- <b>S</b> peed
DP	<b>D</b> ynamic <b>P</b> rogramming
EDU	<b>E</b> lectric <b>D</b> rive <b>U</b> nit
EMF	<b>E</b> lectromotive <b>M</b> otive <b>F</b> orce
FEM	<b>F</b> inite <b>E</b> lement <b>M</b> ethod
FWD	<b>F</b> ront- <b>W</b> heel- <b>D</b> rive
GaN	<b>G</b> allium <b>N</b> itride
HIL	<b>H</b> ardware- <b>I</b> n-the- <b>L</b> oop
ICE	<b>I</b> nternal <b>C</b> ombustion <b>E</b> ngine
IGBT	<b>I</b> nsulated <b>G</b> ate <b>B</b> ipolar <b>T</b> ransistor
IM	<b>I</b> nduction <b>M</b> achine
IPMSM	<b>I</b> nterior <b>P</b> ermanent <b>M</b> agnet <b>S</b> ynchronous <b>M</b> otor
LUT	<b>L</b> ook- <b>U</b> p <b>T</b> able
MOSFET	<b>M</b> etal <b>O</b> xide <b>S</b> emiconductor <b>F</b> ield <b>E</b> ffect <b>T</b> ransistors
MPC	<b>M</b> odel <b>P</b> redictive <b>C</b> ontrol
MTPA	<b>M</b> aximum- <b>T</b> orque- <b>P</b> er- <b>A</b> mpere
NEDC	<b>N</b> ew <b>E</b> uropean <b>D</b> riving <b>C</b> ycle
PMSM	<b>P</b> ermanent <b>M</b> agnet <b>S</b> ynchronous <b>M</b> otor
RWD	<b>R</b> ear- <b>W</b> heel- <b>D</b> rive
SiC	<b>S</b> ilicon <b>C</b> arbide
SoC	<b>S</b> tate of <b>C</b> harge
WBG	<b>W</b> ide <b>B</b> and <b>G</b> ap

WLTC **W**orldwide **H**armonized **L**ight **V**ehicles **T**est **C**ycle



# 1 Introduction

## 1.1 Motivation

The global landscape of transportation is undergoing a transformative shift. As the world grapples with the escalating threats of climate change, there is a pressing need to transition towards more sustainable modes of transportation. Battery electric vehicles (BEVs) have emerged as a beacon of hope in this context. Their promise lies not just in their zero tailpipe emissions, but also in their potential to significantly reduce equivalent life-cycle CO<sub>2</sub> emissions [1, 2], making them a more environmentally friendly alternative to conventional internal combustion engine (ICE) vehicles.

This global trend towards electrification is evident in the rising sales numbers of BEVs as depicted in Figure 1.1. As more consumers become environmentally conscious and governments around the world implement stricter emission regulations, the demand for BEVs continues to surge. However, this transition is not without its challenges. One of the most significant barriers to widespread BEV adoption is the phenomenon commonly referred to as "range anxiety" [3]. This term encapsulates the fear that a BEV will run out of charge before reaching its destination or a charging station. This anxiety primarily stems from the current limitations in battery energy density, particularly lithium-ion ones [4]. While significant advancements have been made in recent years, the energy density of batteries remains a bottleneck, restricting the driving range of BEVs. As a result, the automotive industry has shifted its focus towards optimizing the driving range within these constraints.

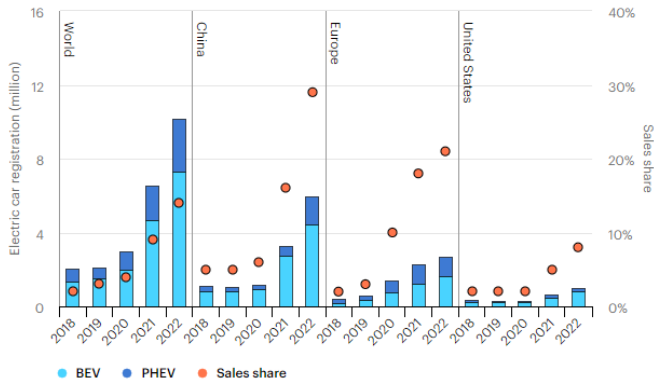


Figure 1.1: *Electric car registrations and sales share in China, United States and Europe, 2018-2022. [5]*

BEVs are driven by electric powertrains that convert the chemical energy stored in the battery to mechanical energy to propel the vehicle. An efficient powertrain can make

the most of the available battery capacity by minimizing energy losses in the powertrain, which stands as a crucial factor in amplifying the driving range. This underscores the indispensable role of powertrain energy efficiency improvement in the broader context of BEV adoption and sustainability.

## 1.2 Electric powertrain energy efficiency

As depicted in Figure 1.2, a conventional electric powertrain for BEV primarily consists of an inverter, which acts as a bridge by converting the battery's direct current (DC) into three-phase alternating current (AC) suitable for the electric motor. This current then powers a three-phase AC motor to produce mechanical torque. The motor, in turn, is coupled to the wheel assembly through a transmission that adjusts the output speed and torque to a suitable range at the wheels. At each stage of energy conversion, energy losses occur, challenging the energy efficiency of the powertrain.

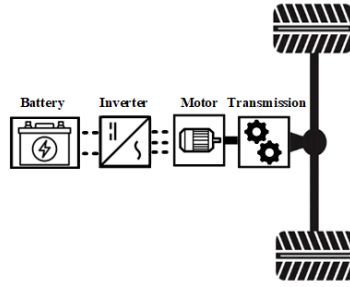


Figure 1.2: *Conventional BEV powertrain structure.*

A BEV powertrain Sankey diagram, as shown in Figure 1.3, provides a comprehensive visualization of these losses and components' efficiencies during both the propulsion and regeneration phases. During the propulsion phase, where the vehicle is powered by the battery, several sources of energy loss are present. The inverter incurs losses primarily due to switching and conduction while converting DC to AC. The electric motor experiences losses from factors like core losses, resistive losses in windings, and mechanical frictions. As the energy flows through the transmission and differential, mechanical losses arise due to frictions between moving components. Moreover, external factors such as aerodynamic drag, tire rolling resistance, and other frictional forces contribute to energy losses, reducing the amount of energy effectively converted to kinetic energy for vehicle movement.

The regeneration braking, an advantageous feature of electric vehicles not found in traditional ICE vehicles, recuperates a portion of the kinetic energy back to battery chemical energy stored in the battery for later use. During the regeneration phase, the energy flows reversely with the electric motor serving as a generator. Similar to the propulsion phase, energy losses arise during each energy conversion stage.

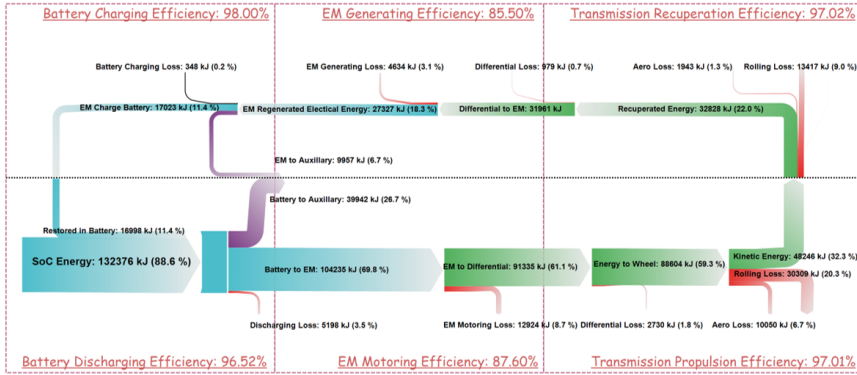


Figure 1.3: *Sankey diagram of a conventional BEV powertrain under a specific drive cycle.*

## 1.3 Related works

Over the years, the drive to enhance the energy efficiency of the BEV powertrain has gained considerable momentum. In light of this, a significant number of innovations and dedicated research efforts have been channeled into both individual components and the powertrain as an integrated system. These efforts can be broadly classified into component-level enhancements and systematic powertrain optimizations as depicted in Figure 1.4.

### 1.3.1 Component-level optimization

The emphasis on individual components in the BEV powertrain has been a defining aspect of numerous research initiatives, leading to state-of-the-art solutions that enhance component-level efficiency. In the area of inverters, works by Nisch et al. [6] and Amirpour et al. [7] have pointed out the benefits of wide band gap (WBG) semiconductor power devices. In particular, inverters using silicon carbide (SiC)-based metal-oxide-semiconductor field-effect transistors (MOSFETs) have been shown to reduce losses by about 50% when compared to those using Si-based insulated gate bipolar transistors (IGBTs), attributed to their improved blocking voltage and reduced switching losses. Parallel to these advancements in inverters, innovations in electric motors have also seen significant progress. One notable advancement is the adoption of high slot-filled ratio windings with rectangular wires or hairpin windings. As indicated by Dimier et al. [8] and Jung et al. [9], hairpin windings, compared to traditional round wires, enable a 15% to 20% increase in slot fill factor [10]. This design advantage results in higher torque output and a substantial reduction of DC copper losses, e.g., the total copper losses in the hairpin permanent magnet synchronous motors (PMSMs) are 16% lower than in the round-wire PMSM at the nominal operating point [11]. Furthermore, considerable effort has been dedicated to refining lubricants and greases for the transmission within electrified powertrains to minimize frictional losses to match the high-speed operation of electric motors [12]. As the trend shifts towards integrating oil-cooled electric motors and

possibly oil-cooled inverters with the transmissions, the dedicated lubricant taking into account the specific demand of electrified powertrains such as heat transfer and insulation characteristics can further enhance the overall powertrain energy efficiency [13, 14].

### 1.3.2 System-level approach

The second area adopts a more holistic perspective, viewing the powertrain as an interconnected system. An increasing number of researchers and industry experts are delving into innovative powertrain configurations. These configurations, equipped with extended degrees of freedom on design and control, can achieve energy efficiencies beyond what's possible with the conventional single motor setup as depicted in Section 1.2.

A notable direction is the exploration of multi-motor powertrains. In such powertrain systems, torque and power requirements are distributed among multiple motors. By dynamically adjusting this distribution based on varying driving conditions, the overall powertrain energy efficiency can be maximized. Among the multi-motor configurations, dual-motor setups have garnered significant attention. In one such configuration, motors are independently placed at the front and rear axles, leading to a 4 - 6% reduction in energy consumption over the New European Driving Cycle (NEDC) [15, 16]. Another prevalent approach integrates two motors through a planetary gear system to drive a single axle. Studies and implementations of this design have also showcased promising improvements in energy efficiency [17–19]. While dual-motor setups have been extensively studied, there's a growing interest in four-motor setups, particularly those utilizing in-wheel motors. Wu et al.[20] highlighted that these four-motor configurations can optimize efficiency similarly to their dual-motor counterparts by intelligently distributing torque among the motors. Moreover, the unique feature of four-wheel independent actuation enables torque vectoring functionality that significantly enhances not only the vehicle cornering maneuverability but also energy efficiency. The reason behind the improved efficiency is the reduction in tire slip power losses and overall powertrain losses. This has been substantiated in studies by Chatzikomis et al. [21] and Dizqah et al. [22], which underscore the potential of four-motor setups in both performance and energy efficiency improvement.

Another exemplary innovative system-level approach integrates multi-speed transmissions. This includes the adoption of two-speed transmissions [23, 24], three-speed variants [25], and even the continuous variable transmission (CVT) [26]. Notably, the commercial viability and performance benefits of such systems are evident in vehicles like the Porsche Taycan [27], which has successfully implemented a two-speed gearbox in its powertrain. Distinct from single-speed transmissions, multi-speed versions can adjust the motor's operating point, thereby optimizing powertrain energy efficiency [28]. As elaborated upon in studies such as [29–31], when the gear ratios and shifting patterns are meticulously designed and harmonized with other powertrain components, the motor can consistently operate within its high-efficiency range across diverse driving conditions. In addition to these advancements, there's also interest in solutions that synergize both multi-motor and multi-speed strategies to push the boundaries of powertrain energy efficiency. For instance, Ruan et al. [32] proposed a dual-motor two-speed (DMTS) drive

system for a single axle, demonstrating a 5 - 8% motor efficiency improvement across various drive cycles. Similarly, another study by Ruan et al. [33] introduced a DM-2ST powertrain configuration, where one motor drives the front axle and a second motor, paired with a 2-speed transmission, drives the rear axle. This configuration exhibited an impressive powertrain energy efficiency improvement of up to 9.13% in the worldwide harmonized light vehicles test cycle (WLTC) compared to the single-speed front and rear axle driven powertrain.

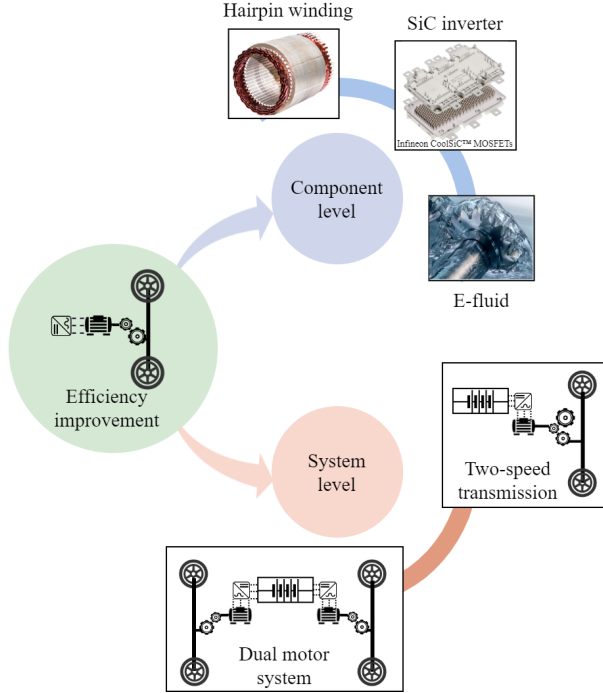


Figure 1.4: *The component level and system level approaches to improve BEV powertrain energy efficiency with examples. [34–36]*

## 1.4 Objectives

The objective of this project is to explore the potential benefits of varying powertrain system configurations as well as the advancement of individual components. Further, this project aims to intricately integrate and utilize both aspects to maximize powertrain energy efficiency. To achieve this, the project employs a methodology anchored in simulation-based studies. This approach requires the modeling of complete powertrains with detailed component losses captured, the development of appropriate control strategies for subsystems and the establishment of a supervisory control for the entire powertrain. Ultimately, highly efficient electric powertrain designs should be proposed.





## 2 Background

### 2.1 Drive cycles

Drive cycles, which can either be statistical representations of typical driving behavior or actual speed-time traces from real-world driving, are pre-defined time-speed profiles. They are crafted to emulate real-world driving conditions and serve as a benchmark for evaluating the performance, fuel efficiency, and emissions of automotive powertrains. In the context of powertrain system simulation, these standard drive cycles offer a structured and repeatable framework for testing and validation, playing a crucial role in calibrating models, optimizing control strategies, and ensuring that simulated outcomes are representative of real-world performance.

For a long time, the NEDC served as the standard reference for vehicle certification but has been criticized for its inability to accurately represent real-world driving patterns. Real-world driving often involves more abrupt changes in speed and acceleration, resulting in higher emissions and fuel consumption than what the NEDC predicts. To address these shortcomings, the WLTC was introduced in 2017 as a replacement for the NEDC [37, 38]. The WLTC was formulated based on real driving data collected from various global regions, including Europe, the United States, Japan, Korea, and India. It offers three different classes of driving cycles tailored to the capabilities of different vehicles, considering factors like power-to-mass ratio and maximum speed [39]. For most passenger cars, the relevant class is class 3 (as shown in Figure 2.1), which spans 30 minutes and includes four distinct speed regions: low, medium, high, and extra-high speed.

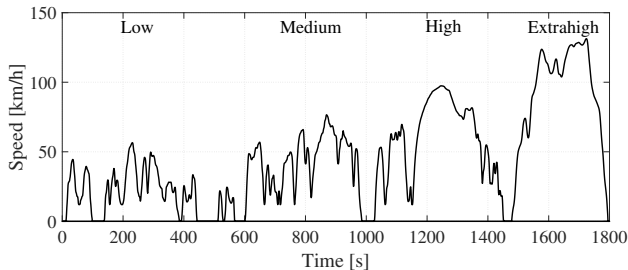


Figure 2.1: *WLTC vehicle speed profile.*

### 2.2 Powertrain system simulation

The powertrain system simulation technique enables the testing of multiple design variations and boundary conditions virtually to optimize the powertrain for performance, efficiency, and reliability. In general, the powertrain system simulation techniques can be categorized by the direction of energy flow: backward simulation and forward simulation [40, 41].

- **Backward simulation:** In backward simulation models, inputs such as vehicle speed and road grade are used to determine wheel torque and speed based on longitudinal vehicle dynamics. By employing kinematic relationships between various powertrain components, the computational process proceeds in a reverse direction, propagating from the wheel, through the transmission, to the engine/electric motor as opposed to the actual flow of energy in the real world (shown in Figure 2.2).

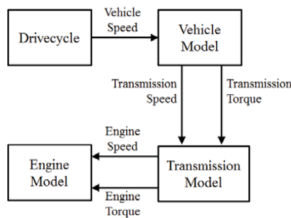


Figure 2.2: *Information flow of backward simulation.* [42]

However, backward simulation has its drawbacks. One key assumption is that the power demand will always be met, which may not be realistic in scenarios like hard acceleration, where the required power could surpass what the powertrain can deliver. Additionally, the absence of a driver model means that brake and throttle signals are not included, complicating the development of control systems.

- **Forward simulation:** In forward simulation models, a driver model is implemented, often as a PI controller. This model compares the target vehicle speed with the actual speed to generate throttle and brake commands. These commands are then converted into a torque request for the engine/motor. The torque passes forward from the engine/electric motor to the wheels through the powertrain, with the same direction of the power flow as reality (shown in Figure 2.3).

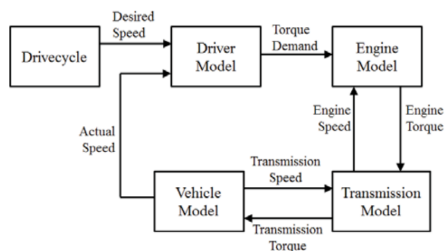


Figure 2.3: *Information flow of forward simulation.* [42]

The presence of a driver model allows for measurable quantities like brake and throttle signals, as well as the torque output. This enables the implementation and testing of vehicle controllers in simulations. Additionally, dynamic models, such as transient effects of power electronics, can be incorporated. Importantly, forward simulation ensures that the power delivered to the wheels will not exceed the

powertrain’s capabilities. However, forward simulation involves extensive integration, requiring relatively small time steps to ensure stable and accurate results. This leads to slower simulation speeds and higher computational power demands.

## 2.3 Powertrain energy management strategy

In electric powertrains, the supervisory controller plays a crucial role in determining the operation of various powertrain components, especially as the complexity of the powertrain configurations grows with numerous degrees of freedom to coordinate each component. Its primary objective is to meet the driving power/torque demand of the vehicle while adhering to various constraints. These constraints can arise from driveability requirements and the inherent characteristics of the individual components such as maximum electric motor torque limit. To achieve this, proper energy management strategies are adopted to orchestrate the energy distribution among the different powertrain components. This ensures that each component operates optimally, fulfilling driving demands and enhancing the overall efficiency and performance of the powertrain.

### 2.3.1 Heuristic strategy

Heuristic energy management strategies are based on intuitive rules and correlations that consider various vehicle variables and are implemented by means of map-based and rule-based approaches. The strategies are often established based on a set of criteria defined by the system, engineering experience, pre-defined driving cycles and even simplified mathematical models. In the map-based approach, the output setpoints are stored in pre-calculated multi-dimensional maps or look-up tables (LUT) whose entries are measured quantities describing the state of the powertrain (such as vehicle speed, state of charge (SoC) and driver power/torque request and vehicle acceleration) [43, 44]. In the rule-based approach, the energy management strategies often employ finite state machines to determine the operation of the powertrain. Each state in this machine corresponds to a distinct mode of the powertrain such as transmission gear numbers and the number of the activated motors. The shifts between states are executed when the predefined conditions are met [45]. The heuristic strategies are straightforward and suitable for real-time implementation. However, the effectiveness largely depends on the careful selection of thresholds and maps that dictate mode switches, which can vary significantly based on driving conditions. If properly tuned, they can yield satisfactory results in energy efficiency. But most often, they do not guarantee optimal results, making it difficult to assess the powertrain efficiency potential of the investigated designs.

### 2.3.2 Dynamic programming

Apart from heuristic strategies, optimization-based strategies such as Dynamic Programming (DP) and online methods like Model Predictive Control (MPC), are pivotal for determining optimal control actions either through global or local optimization techniques, often aimed at minimizing energy consumption. The online methods, though practical when driving conditions are unpredictable, often yield locally optimal solutions.

Conversely, offline methods require prior knowledge of the entire driving cycle, serving as valuable benchmarking tools by providing insights into the given powertrain's maximum potential with globally optimal solutions.

Given the focus of this study on examining the efficiency potential of different powertrain designs, DP with its ability to provide globally optimal results while accommodating multiple constraints on both the input and state side [46, 47] becomes invaluable. It allows for a comprehensive assessment of the efficiency potential of each powertrain configuration, ensuring that evaluations and comparisons are rooted in their maximum achievable powertrain efficiency.

DP primarily emerges from Bellman's principle of optimality. This approach dissects a larger optimization challenge into smaller, more manageable sub-problems and addresses each in a methodical manner [48, 49].

A system in discrete time can be illustrated as:

$$x_{k+1} = f_k(x_k, u_k) \quad (2.1)$$

where  $x_k$  is the the system states and  $u_k$  is the control action/variables at time step  $k$   $0, 1, 2, \dots$ . Both the system states and control actions have constraints:  $x_k \in X_k$  and  $u_k \in U_k$ .

Given a control policy spanning  $N$  time steps as  $u = [u_0, u_1, u_2, \dots, u_{N-1}]$ , the cumulative cost from an initial state  $x_0$  can be expressed as:

$$J(x_0, u) = L_N(x_N) + \sum_{k=1}^{N-1} L_k(x_k, u_k) \quad (2.2)$$

The optimal cost function is then given by:

$$\min_u J(x_0, u) \quad (2.3)$$

with the optimal control policy as  $u = [u_0^*, u_1^*, u_2^*, \dots, u_{N-1}^*]$ .

Considering the sub-problem of minimizing the cost to go from time step  $i$  to  $N$ , the cost is represented as:

$$Y(x_i, i) = L_N(x_N) + \sum_{k=i}^{N-1} L_k(x_k, u_k) \quad (2.4)$$

where  $Y(x_k, k)$  is the optimal cost to go from time step  $k$  to the end with optimal solution  $[u_i^*, u_{i+1}^*, \dots, u_{N-1}^*]$  as per Bellman's principle.

At a specific time instance, the cost associated with a state depends on the control action and the state itself. In the DP framework, the initial procedure requires discretizing states and control inputs throughout the entire time domain. By proceeding backward in time, from time step  $N - 1$  to 1. The end cost is then obtained as:

$$J_N = L_N(x_N) \quad (2.5)$$

The cost-to-go at each intermediate time step can be computed as:

$$J_k(x_k) = \min_u (L_k(x_k, u_k) + J_{k+1}(f_k(x_k, u_k))) \quad (2.6)$$

where  $L_k(x_k, u_k)$  is the cost arising from the state and its associated control action. The subsequent state, after applying this control action, has its own inherent cost-to-go. The cost-to-go conveys the minimal cost to progress from a given state to the final point. If for all  $x_k$  and  $k$ ,  $u_k^o = u_k^o(x_k)$  reduces the right side of the prior equation, the strategy  $[u_0^o, \dots, u_{N-1}^o]$  is the optimal approach.



# 3 Modeling

## 3.1 Longitudinal vehicle dynamics

The powertrain generates tractive force to propel the vehicle and overcome various driving resistances including gradient resistance, aerodynamic resistance, tire rolling resistance, and the force required for acceleration as depicted in Figure 3.1. For the purposes of energy consumption and powertrain operation analysis within this thesis, certain complexities can be simplified. The vehicle is represented as a rigid body, with its mass concentrated at its center of gravity [49]. The focus is solely on the dynamics in the longitudinal direction, under the assumption that the vehicle's stability remains uncompromised. According to Newton's second law, the relationship between these resistances and the traction force produced by the powertrain at each time instant  $t$  can be represented by the following equation:

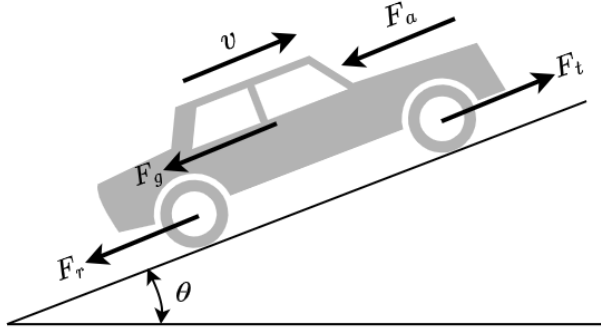


Figure 3.1: Illustration of forces acting on vehicle longitudinal direction.

$$m \frac{d}{dt} v(t) = F_t(t) - (F_a(t) + F_r(t) + F_g(t)) \quad (3.1)$$

where  $m$  is the total equivalent vehicle mass including inertias of rotating components in the powertrain,  $\frac{d}{dt} v(t)$  is the vehicle acceleration,  $F_a(t)$  is the aerodynamic drag force,  $F_r(t)$  is the tire rolling resistance force and  $F_g(t)$  is the road gradient force. The derivation of these forces is discussed as follows.

- **Tractive Force ( $F_t$ ):** The tractive force refers to the main force responsible for propelling or decelerating a vehicle. Contrary to its name, the tractive force can be positive, negative, or even zero, depending on the vehicle's state. During the propulsion phase, the tractive force is positive. It originates from the electric motor(s) and is transmitted through the transmission to the contact area between the wheels and the road. In the event of braking, the tractive force becomes negative. The motor works as a generator to decelerate the vehicle, simultaneously regenerating electricity. In cases of extreme deceleration, both the frictional brake and the electric motor contribute to the negative tractive force. Conversely, during

cruising or what is termed as a free-rolling event, the tractive force is zero, indicating that the powertrain isn't delivering any active mechanical power.

- **Aerodynamic drag force ( $F_a$ ):** The aerodynamic drag force, experienced by a moving vehicle is influenced by the vehicle's intricate shape and the complex nature of fluid dynamics (e.g. the viscous friction between the vehicle's surface and the surrounding air). A widely accepted approach employs a partly empirical model with a pronounced dependence on the square of the vehicle speed. For computational purposes, vehicles are often represented as prismatic bodies with a frontal area. The force is then adjusted by an aerodynamic drag coefficient to approximate real flow conditions. The aerodynamic drag force is thus formulated as:

$$F_a = \frac{1}{2} \rho_{\text{air}} C_d A_f v^2 \quad (3.2)$$

where  $\rho_{\text{air}}$  is the air density,  $C_d$  is the aerodynamic drag coefficient,  $A_f$  is the vehicle frontal area and  $v$  is the vehicle speed.

- **Tire rolling resistance force:** The rolling resistance force,  $F_r$ , arises due to the deformation of the tire as it rolls on the road surface which can be modeled as:

$$F_r = C_r mg \cos(\theta) \quad (3.3)$$

where  $C_r$  is the tire rolling resistance coefficient,  $g$  is the gravitational acceleration and  $\theta$  is the road inclination angle.

- **Road gradient force:** The road gradient force arises due to the inclination or decline of the road surface. When a vehicle travels uphill, additional force is required to overcome the gravitational component pulling the vehicle back down. Conversely, when descending, this force can assist in propelling the vehicle forward. The road gradient force can be mathematically represented as:

$$F_g = mg \sin(\theta) \quad (3.4)$$

The main vehicle parameters used in this study can be found in Table 3.1.

Table 3.1: Main vehicle parameters.

Parameters	Description	Value	Unit
$m$	Vehicle mass	2640	kg
$C_d$	Aerodynamic resistance coefficient	0.372	-
$A_f$	Frontal area	2.8	m <sup>2</sup>
$R_r$	Tire rolling radius	377	mm
$C_r$	Tire rolling resistance coefficient	0.01	-



### 3.2 Battery

To capture the dynamic behavior of the battery and the corresponding variations in the terminal output under different operating conditions, the battery can be modeled simply as an equivalent electric circuit consisting of an open circuit voltage  $V_{oc}$  and an internal resistance  $R_i$  [50–52], as depicted in Figure 3.2. The open circuit voltage and internal resistance are often tabulated against the SoC (and possibly temperature), using curve-fitting techniques based on experimental measurements for both the charging and discharging processes as depicted in Figure 3.3.

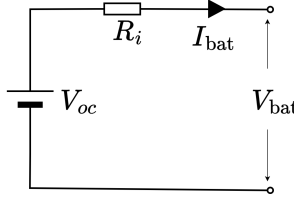


Figure 3.2: *Battery equivalent circuit model.*

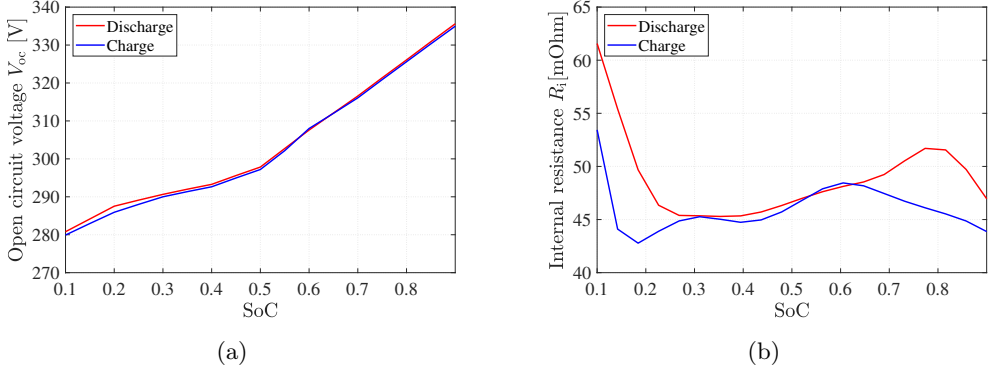


Figure 3.3: *Battery (pack level) data tested under charge and discharge conditions: (a) open circuit voltage and (b) internal resistance.*

The battery state of charge can be calculated as:

$$\text{SoC}(t) = \text{SoC}(t_0) + \int_{t_0}^t \frac{1}{C_{\text{bat}}} \frac{V_{oc} - \sqrt{V_{oc}^2 - 4R_i P_{\text{bat}}(t)}}{2R_i} dt \quad (3.5)$$

where  $\text{SoC}(t_0)$  is the initial battery SoC,  $C_{\text{bat}}$  is the battery capacity, and  $P_{\text{bat}}$  is the terminal output power of the battery.

The battery power loss due to the presence of internal battery resistance can be described as follows:

$$P_{\text{bat,loss}} = I_{\text{bat}}^2 R_i \quad (3.6)$$

where  $I_{\text{bat}}$  is the battery current.

The terminal voltage  $V_{\text{bat}}$ , which is the voltage at the battery terminals, is influenced by the internal resistances and the battery current. The relationship can be expressed as:

$$V_{\text{bat}} = V_{\text{oc}} - I_{\text{bat}} R_i \quad (3.7)$$

The battery terminal power can be written as:

$$P_{\text{bat}} = (V_{\text{oc}} - I_{\text{bat}} R_i) I_{\text{bat}} \quad (3.8)$$

### 3.3 Electric motor

There is a myriad of electric motor types suitable for electric vehicle applications as listed in Figure 3.4. Among these, This study preliminary focuses on Interior Permanent Magnet Synchronous Motor (IPMSM) with superior power density and efficiency, making it a dominant choice in the current BEV market [53, 54].

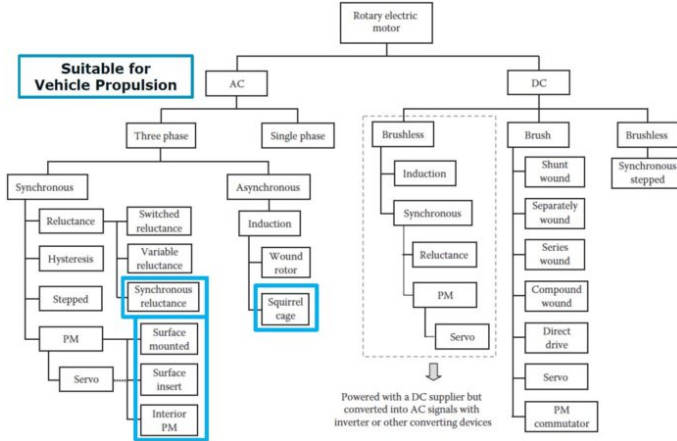


Figure 3.4: *Electric motor types with “Suitable for vehicle propulsion” highlighted by AVL. [55]*

In the context of synchronous machines, the d-q axis representation, specifically in the rotor frame of reference, offers a more intuitive understanding of the motor’s dynamics. The direct axis, or d-axis, physically corresponds to a radial axis that intersects the centerline of the magnets, representing the direction of the magnetic flux emanating from a magnet. On the other hand, the quadrature axis, or q-axis, aligns between two magnets (or between two magnetic poles) and is positioned 90 electrical degrees ahead of the d-axis. This transformation simplifies the analysis by converting the three-phase system into a stationary two-phase system in synchronous coordinates.

Figure 3.5 shows the equivalent electric circuit model of PMSM under the d-q frame.

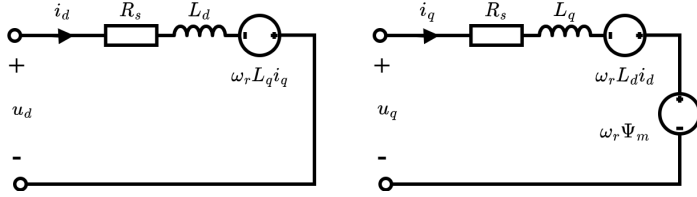


Figure 3.5: PMSM equivalent electric circuit model.

The dynamic stator voltage equations for the d- and q-axes, can be expressed as:

$$u_d = R_s i_d + L_d \frac{di_d}{dt} - \omega_r L_q i_q + \omega_r \Psi_m \quad (3.9)$$

$$u_q = R_s i_q + L_q \frac{di_q}{dt} + \omega_r L_d i_d \quad (3.10)$$

where  $u_d$  is the d-axis stator voltage,  $u_q$  is the q-axis stator voltage,  $R_s$  is the stator resistance,  $L_d$  is the d-axis inductance,  $L_q$  is the q-axis inductance,  $\omega_r$  is the electrical speed of the rotor and  $\psi_m$  is the magnet flux linkage.

For salient machines such as the IPMSM, where  $L_d \neq L_q$ , the produced torque  $T_e$  consists of both the magnet torque and the reluctance torque as:

$$T_e = \frac{3}{2} n_p (\Psi_m i_q + (L_d - L_q) i_d i_q) \quad (3.11)$$

where  $n_p$  is the number of pole pairs.

For a Permanent Magnet Synchronous Motor (PMSM), the primary losses include the copper loss, which results from the resistance of the stator windings; the iron (core) loss, originating from both the stator and rotor; and mechanical losses from the moving components.

- **Copper loss:** Copper losses in a PMSM are induced by the stator winding phase resistance  $R_s$  and can be expressed as:

$$P_{cu} = \frac{3}{2} R_s I_{s,\text{rms}}^2 = \frac{3}{2} R_s (i_d^2 + i_q^2) \quad (3.12)$$

where  $I_{s,\text{rms}}$  is the root-mean-square stator phase current. The resistance  $R_s$  is temperature-dependent. The resistance  $R_s$  can be further broken down into  $R_{dc}$  and  $R_{ac}$  to account for DC and AC copper losses. While DC losses are relatively straightforward and arise from the resistance of the windings, AC losses are more intricate where the ratio  $\frac{R_{ac}}{R_{dc}}$  is proportional to the motor speed and  $I_{s,\text{rms}}$  [56].

The AC loss results from phenomena like the skin effect, where the current tends to flow on the outer surface of the conductor, and the proximity effect, where the current distribution is affected by the magnetic field of adjacent conductors. Figure 3.6 shows the non-uniform current distribution in hairpin windings during high-frequency operation. These effects make AC losses challenging to capture analytically, thus Finite Element Method (FEM) simulations, are often employed to accurately estimate copper losses.

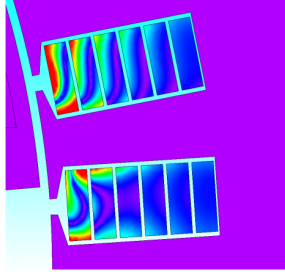


Figure 3.6: *Current density distributions in copper windings at high frequency operation.* [9]

- **Iron loss:** Iron losses, also known as core losses, are primarily attributed to magnetic hysteresis and induced eddy currents. The average iron losses can be represented as:

$$P_{fe} = k_h f \hat{B}^n + k_e f^2 \hat{B}^2 \quad (3.13)$$

where  $f$  is the supplied voltage frequency,  $\hat{B}$  is the peak magnetic flux density,  $n$  is the hysteresis exponent, and  $k_h$  and  $k_e$  are hysteresis and eddy current coefficients, respectively. However, real-world excitations, especially in electric drive systems, might not always be purely sinusoidal due to the presence of harmonics, switching effects, etc. In such cases, the actual iron losses can be different from those predicted under pure sinusoidal excitation. To account for these discrepancies, a scaling factor in the range of 1.5 - 2 is often applied to the iron losses calculated based on pure sinusoidal excitation.

- **Mechanical loss:** Mechanical losses mainly comprise two categories: friction losses and windage or airgap losses. The friction losses predominantly originate from the rotor bearings and their lubrication system. On the other hand, windage losses result from the air resistance encountered as the rotor rotates. Both losses are speed-dependent, increasing as the rotational speed of the rotor rises.

### 3.4 Converters

The switched-mode converters regulate the flow of energy between the battery, electric motor and other electrical components. They can either convert DC to AC which drives the motor or adjust DC voltage levels to cater to different operational needs.

Two primary transistors investigated in this study are the IGBT paired with anti-parallel diodes and SiC MOSFETs. In the rest of thesis, SiC MOSFET will simply be referred to as MOSFET, as Si-MOSFET is not considered in the study. IGBTs are known for their high input impedance and low saturation voltage, making them suitable for various power electronic applications. SiC MOSFETs, on the other hand, come with the advantage of reverse conduction capability, eliminating the need for parallel diodes and offering more efficient operation. Both these devices, while crucial for the powertrain efficiency, come with inherent losses. Conduction losses occur when the device is in the 'on' state while switching losses arise during the transition between 'on' and 'off' states. In the case of diodes, the turn-on losses are often disregarded due to the rapid turn-on process inherent to these components. While losses stemming from the driver and snubber circuits, as well as those due to capacitive and inductive parasitics, are considered minimal and thus neglected [57].

### 3.4.1 DC-DC converter

A DC-DC converter can be potentially used as an intermediary between the battery and the DC-link [58–60], realized by a bidirectional boost DC-DC converter, as shown in Figure 3.7. This arrangement allows for voltage boosting from the battery to the DC-link and voltage stepping down from the three-phase inverter back to the battery. These operations align with the propulsion and regenerative braking modes of electric vehicles, respectively.

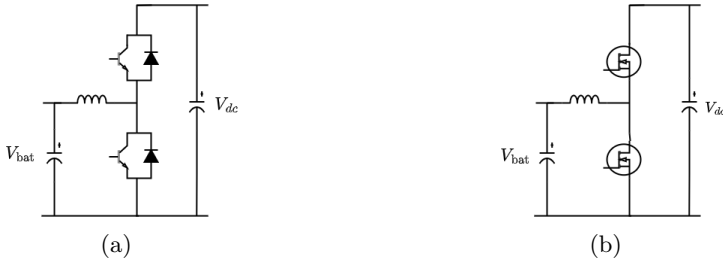


Figure 3.7: Bidirectional boost DC-DC converter: (a) with IGBTs and (b) with MOSFETs.

For an IGBT-based DC-DC converter, the losses can be calculated analytically as follows [61, 62]:

$$\begin{aligned}
 P_{\text{DCDC,loss,IGBT}} &= P_{\text{cond,IGBT}} + P_{\text{cond,diode}} + P_{\text{sw,IGBT}} + P_{\text{sw,diode}} \\
 &= (V_{ce0}I_{\text{bat}} + r_{ce}I_{\text{bat}}^2) D + (V_{d0}I_{\text{bat}} + r_dI_{\text{bat}}^2) (1 - D) \\
 &\quad + E_{\text{sw}}f_{\text{sw}} \left( \frac{I_{\text{bat}}}{I_{\text{ref}}} \right)^{K_{it}} \left( \frac{V_{\text{dc}}}{U_{\text{ref}}} \right)^{K_{vt}} + E_{\text{rec}}f_{\text{sw}} \left( \frac{I_{\text{bat}}}{I_{\text{ref}}} \right)^{K_{id}} \left( \frac{V_{\text{dc}}}{U_{\text{ref}}} \right)^{K_{vd}}
 \end{aligned} \tag{3.14}$$

where  $V_{ce0}$  is the IGBT forward voltage drop,  $r_{ce}$  is IGBT on-state resistance,  $V_{d0}$  is the diode forward voltage drop,  $r_d$  is the diode on-state resistance,  $V_{\text{dc}}$  is DC-link voltage,  $f_{\text{sw}}$

is the switching frequency,  $I_{\text{ref}}$  is the reference current used for linearizing the switching loss,  $U_{\text{ref}}$  is the reference voltage used for linearizing the switching loss,  $E_{\text{sw}}$  is transistor switching energy loss as the sum of turn-on loss  $E_{\text{on}}$  and turn-off loss  $E_{\text{off}}$ ,  $E_{\text{rec}}$  is the diode reverse recovery energy,  $K_{it}$  is the coefficient used for describing the transistor switching loss dependency on current,  $K_{vt}$  is the coefficient used for describing the transistor switching loss dependency on voltage,  $K_{id}$  is the coefficient used for describing the diode switching loss dependency on current and  $K_{vd}$  is the coefficient used for describing the diode switching loss dependency on voltage.

In addition,  $D$  is the duty cycle and can be calculated as:

$$D = \begin{cases} \frac{V_{\text{bat}}}{V_{\text{dc}}} & \text{buck operation} \\ 1 - \frac{V_{\text{bat}}}{V_{\text{dc}}} & \text{boost operation} \end{cases} \quad (3.15)$$

Due to the reverse conduction capability of MOSFETs, the MOSFETs operate differently compared to IGBTs paired with anti-parallel diodes during the reverse conduction period depending on the current condition [63–65]. For this study, the voltage drop across the transistor on-state resistance,  $r_{ds}$ , is always smaller than the forward voltage drop of the body diode,  $V_{sd0}$  as:

$$I_{\text{bat}} \cdot r_{ds} < V_{sd0} \quad (3.16)$$

Therefore, it can be assumed that the body diodes of the MOSFETs do not conduct the reverse current during the reverse conduction period, hence the conduction losses only occur on the transistors. For a MOSFET-based DC-DC converter, the losses can be calculated analytically as follows:

$$\begin{aligned} P_{\text{DCDC,loss,MOSFET}} &= P_{\text{cond,MOSFET}} + P_{\text{sw,MOSFET}} \\ &= r_{ds} I_{\text{bat}}^2 + 2E_{\text{sw}} f_{\text{sw}} \left( \frac{I_{\text{bat}}}{I_{\text{ref}}} \right)^{K_{it}} \left( \frac{V_{\text{dc}}}{U_{\text{ref}}} \right)^{K_{vt}} \end{aligned} \quad (3.17)$$

### 3.4.2 DC-AC inverter

Figure 3.8 illustrates the structure of a three-phase inverter consisting of three legs, with each leg containing a half-bridge configuration of two switches. The losses of the inverter can be calculated analytically based on the assumption of an ideal sinusoidal current waveform. For an IGBT-based inverter, the losses can be calculated analytically as follows [61, 62]:

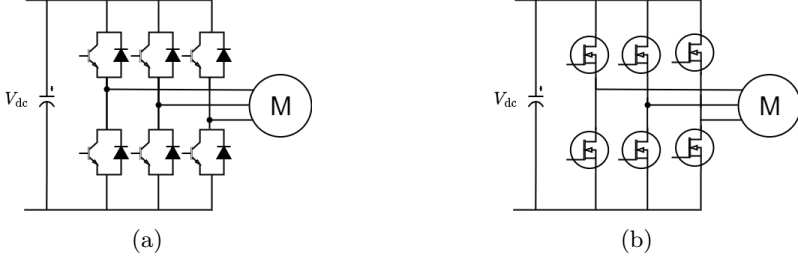


Figure 3.8: *Three-phase inverter: (a) with IGBTs and (b) with MOSFETs.*

$$\begin{aligned}
 P_{\text{inv,loss,IGBT}} &= P_{\text{cond,IGBT}} + P_{\text{cond,diode}} + P_{\text{sw,IGBT}} + P_{\text{sw,diode}} \\
 &= 6V_{ce0}I_o \left( \frac{1}{2\pi} + \frac{M \cos \varphi}{8} \right) + 6r_{ce}I_o^2 \left( \frac{1}{8} + \frac{M \cos \varphi}{3\pi} \right) \\
 &\quad + 6V_{d0}I_o \left( \frac{1}{2\pi} - \frac{M \cos \varphi}{8} \right) + 6r_dI_o^2 \left( \frac{1}{8} - \frac{M \cos \varphi}{3\pi} \right) \\
 &\quad + 6E_{\text{sw}}f_{\text{sw}} \left( \frac{I_o}{\pi I_{\text{ref}}} \right)^{K_{it}} \left( \frac{V_{\text{dc}}}{U_{\text{ref}}} \right)^{K_{vt}} + 6E_{\text{rec}}f_{\text{sw}} \left( \frac{I_o}{\pi I_{\text{ref}}} \right)^{K_{id}} \left( \frac{V_{\text{dc}}}{U_{\text{ref}}} \right)^{K_{vd}}
 \end{aligned} \tag{3.18}$$

where  $I_o$  is the amplitude of AC phase current,  $M$  is the modulation index,  $\cos \phi$  is the power factor.

For a MOSFET-based inverter, the losses can be calculated analytically when MOSFETs' reverse conduction capability is utilized as follows :

$$\begin{aligned}
 P_{\text{inv,loss,MOSFET}} &= P_{\text{cond,MOSFET}} + P_{\text{sw,MOSFET}} \\
 &= \frac{3}{2}I_o^2 r_{\text{ds}} + 6(E_{\text{sw}})f_{\text{sw}} \left( \frac{I_o}{\pi I_{\text{ref}}} \right)^{K_{it}} \left( \frac{V_{\text{dc}}}{U_{\text{ref}}} \right)^{K_{vt}}
 \end{aligned} \tag{3.19}$$

### 3.5 Transmission

The transmission serves to reduce the speed of the electric motor while simultaneously amplifying its torque output, ensuring the speed and torque at the wheels align with the vehicle's operational requirements. Meanwhile, it incurs various losses such as gearing losses, bearing losses and churning losses [66–69]. However, the transmission efficiency is relatively stable unlike the electric motor and inverter, where efficiency can vary significantly across different speed and torque ranges. This characteristic allows for certain simplifications in system-level analyses. For instance, it's common practice to assume a constant efficiency value for the gearbox, streamlining the evaluation process [70, 71].





# 4 Adaptive Front and Rear Axle Independently Driven Powertrain

Dual motor powertrains have emerged as a viable alternative to single motor BEV powertrains, primarily due to their torque distribution capabilities and superior power density [72–74]. Specifically, the front and rear axle independently driven (FRID) powertrain with PMSMs is often adopted by BEV manufacturers due to its exceptional all-wheel-drive performance, fault-tolerance, and structural simplicity [75–77]. However, an electric drive unit (EDU), comprising a gearbox, a PMSM, and an inverter, can experience significant no-load losses during free-spinning scenarios, particularly at higher speeds. These no-load losses can be attributed to i) losses arising from the inverter and PMSM when reactive current is supplied to mitigate the back electromotive motive force (EMF) induced by the permanent magnets in the field weakening domain [78] and ii) losses due to mechanical friction within the EDU rotational parts. As a result, the no-load losses inherent to PMSM-based EDUs can substantially deteriorate the energy efficiency of FRID powertrains, especially when compared to single motor powertrains. This assertion is corroborated by publicly accessible data on current BEVs in the market, as illustrated in Table 4.1. Notably, the Tesla model Y, which comprises one induction machine (IM) in the two motors, the WLTC energy consumption in relation to the single motor variant shows a better trend than that of the Volvo C40 recharge or the Polestar 2 since the IM has low no-load losses.

Table 4.1: WLTC energy consumption of current BEV models with FRID powertrains and single motor powertrain. [79]

Vehicle model	Powertrain	WLTC cons. [kWh/100km]	Reduction
Polestar 2 Long range	Dual PMSMs FRID	19.4	-
	Single PMSM	17.1	11.9%
Tesla Model Y	IM / PMSM FRID	17.0	-
	Single PMSM	15.5	8.8%
Volvo C40 Recharge	Dual PMSMs FRID	20.7	-
	Single PMSM	18.2	12.1%

To further enhance the energy efficiency of FRID powertrains and utilize their operational flexibility, integrating a mechanical disconnect functionality into PMSM-based EDUs could be a promising solution to counteract the inherent no-load losses.

## 4.1 Powertrain configuration

The Adaptive Front and Rear Axle Independently Driven (AFRID) powertrain, as illustrated in Figure 4.1, features two sets of EDUs positioned at the front and rear

drive axles that can be mechanically disengaged to the corresponding drive axle through a dog clutch, as showcased in Figure 4.2. Based on the states of the EDUs and clutches, which are detailed in Table 4.2, the AFRID powertrains can shift among three operating modes: front-wheel-drive (FWD), rear-wheel-drive (RWD), and all-wheel-drive (AWD).

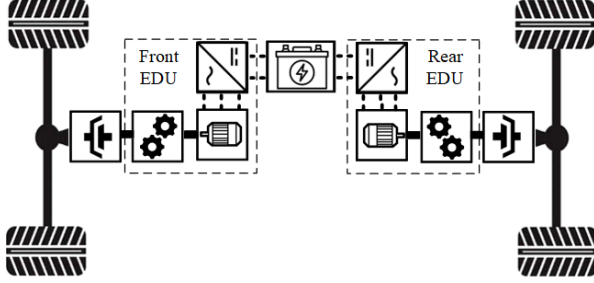


Figure 4.1: *AFRID powertrain structure.*

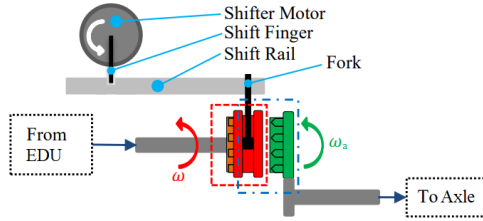


Figure 4.2: *Structure of dog clutch assembly.*

Table 4.2: EDU and clutch engagement states for each operating mode.

Mode	Front EDU	Rear EDU	Front clutch	Rear clutch
FWD	active	inactive	engaged	disengaged
RWD	inactive	active	disengaged	engaged
AWD	active	active	engaged	engaged

The front and rear EDUs equip PMSMs that share the same rotor design but differ in winding topologies. Specifically, the front EDU employs a PMSM with stranded windings, while the rear EDU features a PMSM with hairpin windings. This approach results in differentiated high-efficiency operating areas and similar torque-speed ranges for the front and rear EDUs, enabling the utilization of the efficiency characteristics of each motor according to different driving conditions while maintaining FWD, RWD, and AWD capabilities across the vehicle's entire speed range. Furthermore, this approach avoids the additional manufacturing costs associated with producing two completely different motors. The efficiency maps of the front and rear EDU are shown in Figures 4.3a and 4.3b, respectively.

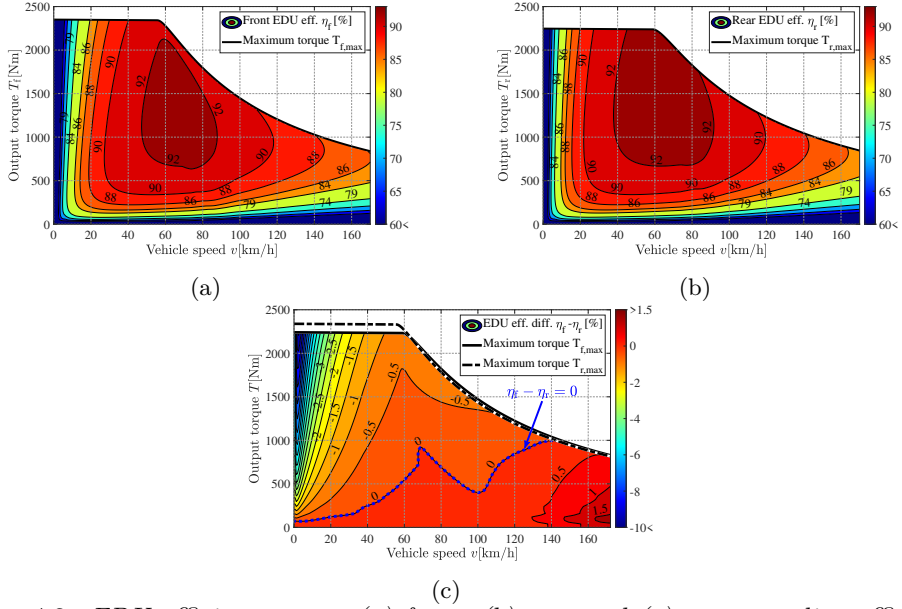


Figure 4.3: *EDU efficiency map: (a) front, (b) rear and (c) corresponding efficiency difference map.*

The front EDU exhibits higher efficiency in high-speed, low-torque operating areas, while the rear EDU is more efficient at lower speeds and high-torque operating conditions. The underlying reason lies in the winding topologies. Hairpin windings in the rear PMSM have a larger cross-section, which minimizes DC copper losses but increases AC copper losses due to a non-uniform current distribution. At low speeds where DC copper losses are dominant, this makes the rear EDU with hairpin windings more efficient compared to the front EDU with stranded windings. However, at higher speeds, AC copper losses scale significantly as frequency increases and further non-uniform current distribution cancels out the benefit of low DC copper losses, thereby reducing the efficiency of the rear EDU [9, 80]. This efficiency difference indicates the two EDUs can be complementary to each other when maximizing the overall powertrain efficiency under different vehicle operating conditions.

## 4.2 Powertrain controller

### 4.2.1 Supervisory controller

A proposed supervisory powertrain controller is depicted in Figure 4.4, designed to utilize the AFRID powertrain's flexible operating modes for maximizing the energy efficiency. This control process is structured into three layers:

- The first layer preliminary determines the desired operating mode based on vehicle speed,  $v$ , and torque demand,  $T_{dem}$ . The specifics of the mode selection strategy

are elaborated in the subsequent section.

- The second layer integrates a 2s hysteresis delay to avoid frequent mode transitions and clutch toggling. However, in case of abrupt high torque demands outside of a single motor's torque constraint, this delay is bypassed, activating the AWD mode instantly.
- In the third layer, a finite state machine processes the mode shift instructions from the preceding layers, coordinating clutch actuation and torque allocation to the EDUs. During mode shift transitions, the relevant EDU speed is controlled to cope with clutch engagement or disengagement, which will be discussed in the following section. Clutch commands, denoted as  $DC$ , are dispatched based on drive axle ( $\omega_a$ ) and EDU speeds ( $\omega$ ) obtained from vehicle sensors. To differentiate between front and rear, the variables are sub-scripted with  $f$  and  $r$  respectively.

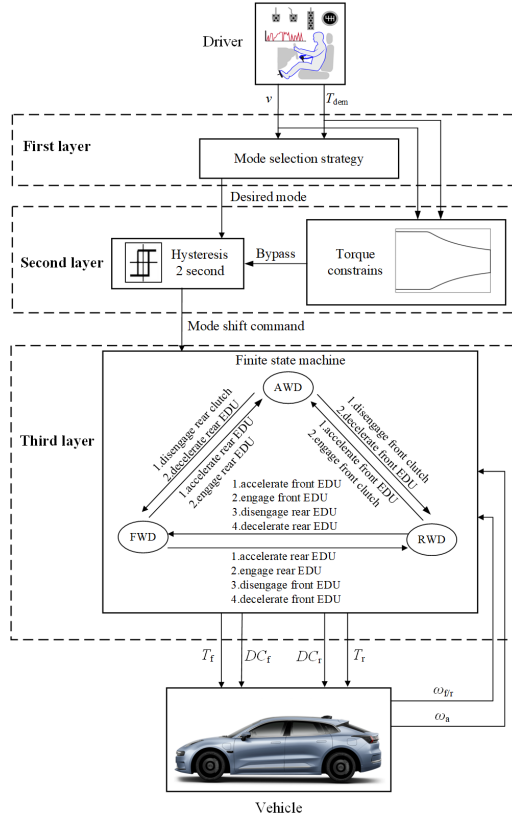


Figure 4.4: AFRID powertrain supervisory controller scheme.

### 4.2.2 EDU speed controller

The dog clutch engagement comprises four phases, as depicted in Figure 4.5. Prior to the engagement, it's imperative to synchronize the rotational speeds of the EDU output shaft with the drive axle. The shifter motor actuates the fork to commence the engagement only when the speed difference,  $|\omega_{diff}|$ , between the two shafts is confined within a specific threshold (12 rpm in this study). This ensures not only a smooth engagement but also reduced wear on the clutch [81, 82].

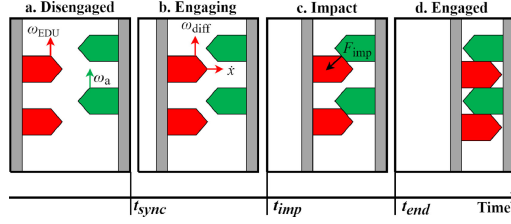


Figure 4.5: *Dog clutch engagement processes.*

During powertrain operating mode shift transitions, the EDU speed controller accelerates the EDU speed to align with the drive axle's rotational speed. Conversely, when the EDU detaches from the drive axle, its speed is decelerated to zero to not only recover kinetic energy but also mitigate no-load losses quickly. The EDU speed is realized by requesting a speed control torque request  $T_{ctr}$  to the EDU to counter the inertia and friction torque  $T_{fric}$  until the EDU reaches the desired speed according to:

$$T_{ctr} = J \frac{d\omega}{dt} + T_{fric} \quad (4.1)$$

where  $J$  is the inertia of the rotational parts.

To ensure fast speed control, a high torque demand up to the maximum and minimum output torque of the EDU, is normally used. However, such a rapid EDU speed control process results in high energy losses in the transient speed control process with EDU not being used efficiently. Given that mode shift transitions aren't typically time-critical in FRID powertrains, an energy-efficient EDU speed control strategy is proposed to minimize the transient energy losses.

The energy-efficient EDU speed control torque is defined as a torque trajectory relative to the EDU speed. As illustrated in Figure 4.6, the speed control torque is updated based on the current EDU speed measurement and in turn sent to the EDU. The energy-efficient control torque is derived as Table 4.3:

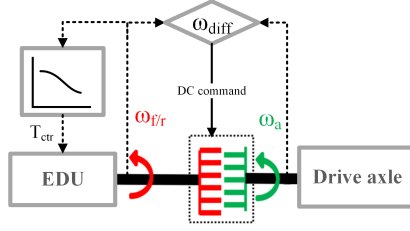


Figure 4.6: The scheme of energy-efficient EDU speed control process.

Table 4.3: Description of energy-efficient EDU speed control torque derivation.

---

Energy-efficient control torque to control EDU speed from initial speed  $\omega_0$  to target speed  $\omega_N$

---

**Step 1: Speed Segmentation**

Segment the speed control process into  $N$  sub-processes:  $[\omega_0, \omega_1]$ ,  $[\omega_1, \omega_2]$ ,  $\dots$ ,  $[\omega_{N-1}, \omega_N]$ .

**Step 2: Control Torque Test Values**

For the acceleration process, generate the control torque test values as  $[0 : 1 : T_{\max}]$ ; For the deceleration process, generate the control torque test values as  $[T_{\min} : 1 : 0]$ .

**Step 3: Speed Propagation in Sub-process**

During each sub-process, the control torque test value  $T_{\text{ctr}}$  is assumed constant. Calculate EDU speed propagation with  $i$  time steps of  $\Delta t = 0.001\text{s}$ :  $\omega_{i+1} = \frac{(T_{\text{ctr}} - T_{\text{fric}}(\omega_i))\Delta t}{J}$  for all the test values and each sub-process.

**Step 4: Energy Loss in Sub-process**

Compute the corresponding energy losses incurred during each sub-process with each control torque test value:  $E_{\text{ctr}} = \sum_{i=1}^N P_{\text{loss},i}(\omega_i, T_{\text{ctr}}) \Delta t$ .

**Step 5: Energy-efficient Control Torque Determination**

For each sub-process, find the control torque test value with minimum energy loss at the corresponding sub-process.

**Step 6: Merge Energy-efficient Control Torque**

Merge energy-efficient control torque for each sub-process to energy-efficient EDU speed control torque  $T_{\text{ctr}}^*$  trajectory for the entire EDU speed control process from  $\omega_0$  to  $\omega_N$ .

---

The derived energy-efficient control torque trajectories to be followed when accelerating or decelerating the EDU can be derived and illustrated in Figure 4.7.

### 4.3 Powertrain operation strategy

The complementary efficiency difference between the front and rear EDU leads to distinct powertrain losses (consisting of front and rear EDU losses) for each operating mode. Consequently, the powertrain energy efficiency can be maximized by the proper selection of the operating mode. Besides, the AWD mode provides an extra degree of freedom, allowing for the minimization of powertrain losses through optimal torque distribution

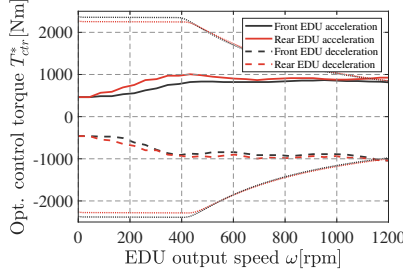


Figure 4.7: *Energy-efficient EDU speed control torque trajectories to be followed when accelerating or decelerating the EDU.*

between the front and rear EDU.

#### 4.3.1 Optimal torque distribution strategy in AWD mode

In the AWD mode, the torque demanded to drive or brake the vehicle can be distributed between the front and rear EDU as:

$$T_{\text{dem}} = T_f + T_r \quad (4.2)$$

where  $T_f$  and  $T_r$  are the torque provided by the front and rear EDU.

For a more structured approach, a torque distribution ratio,  $\alpha$  is introduced. This allows for the representation of  $T_f$  and  $T_r$  as:

$$\begin{cases} T_f = \alpha T_{\text{dem}} \\ T_r = (1 - \alpha) T_{\text{dem}} \end{cases} \quad (4.3)$$

Based on EDUs power losses, an optimal distribution ratio,  $\alpha$ , minimizing the overall losses of both EDUs can be identified. The torque distribution optimization problem can therefore be formalized as follows:

$$J = \min \{ P_{\text{loss},f}(\omega_f, \alpha T_{\text{dem}}) + P_{\text{loss},r}(\omega_r, (1 - \alpha) T_{\text{dem}}) \} \quad (4.4)$$

with the constraints of

$$\begin{cases} T_{f,\min}(\omega_f) \leq \alpha T_{\text{dem}} \leq T_{f,\max}(\omega_f) \\ T_{r,\min}(\omega_r) \leq (1 - \alpha) T_{\text{dem}} \leq T_{r,\max}(\omega_r) \\ \alpha \in [0, 1] \end{cases} \quad (4.5)$$

where  $P_{\text{loss},f}$  is the front EDU loss,  $P_{\text{loss},r}$  is the rear EDU loss,  $T_{f,\min}$  is the minimum torque of the front EDU,  $T_{f,\max}$  is the maximum torque of the front EDU,  $T_{r,\min}$  is the minimum torque of the rear EDU and  $T_{r,\max}$  is the maximum torque of the rear EDU.

For convenience, the vehicle speed is used as the reference speed. Given each pair of vehicle speed and torque demand, the optimal torque distribution ratio,  $\alpha_{\text{opt}}$ , can be determined using an offline grid search method [83, 84]. Figure 4.8 illustrates the optimal torque distribution ratio.

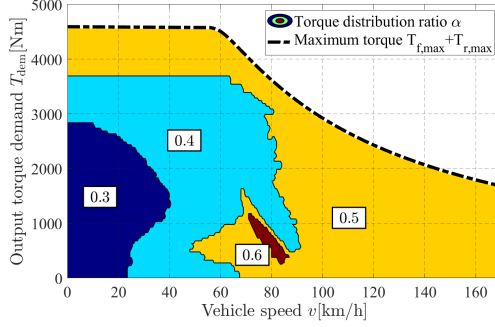


Figure 4.8: *Optimal torque distribution ratio  $\alpha_{\text{opt}}$  in AWD mode.*

### 4.3.2 Powertrain mode selection strategy

The mapped powertrain losses for different operating modes are shown in Figure 4.9. For AWD mode, an optimal torque distribution strategy with  $\alpha_{\text{opt}}$  is taken into account. For FWD and RWD modes, the torque split ratio,  $\alpha$ , is substituted by 1 and 0, respectively. Based on the powertrain losses for different operating modes, the operating mode with minimum powertrain loss (shown in Figure 4.10) can be determined with respect to vehicle speed and torque demand inputs and serve as the guideline for rule-based mode selection strategy.

However, to maximize the energy efficiency of the AFRID powertrain, it is essential to select an optimal operating mode sequence that minimizes total powertrain losses, taking into account the energy losses incurred during mode shift transitions. Given prior knowledge of the vehicle's route where the speed profile is considered known, DP can be utilized for mode selection strategy optimization.

The powertrain operating mode is chosen as the only state variable  $x$  with three possible integer values: 1, 2, and 3 which represent the FWD, RWD, and AWD modes, respectively. Consequently, the control variable, operating mode shift command,  $u$ , which is an integer within the range  $[-2, 2]$ , represents different mode shift commands. The investigated drive cycle is discretized into  $N$  stages in the time span. The time response of the EDU speed control during mode shift transition is mostly within one second except in extreme cases where the EDU speed needs to be accelerated or decelerated between 0 and maximum EDU speed. Thus, one second is an appropriate time step  $\Delta T$ . The powertrain operating mode at stage  $k$ ,  $x_k$ , together with the operating mode shift command,  $u_k$ , determine the new operating mode,  $x_{k+1} = x_k + u_k$ , in the next stage. Infeasible modes ( $x_k \neq 1, 2, 3$ ) are excluded.



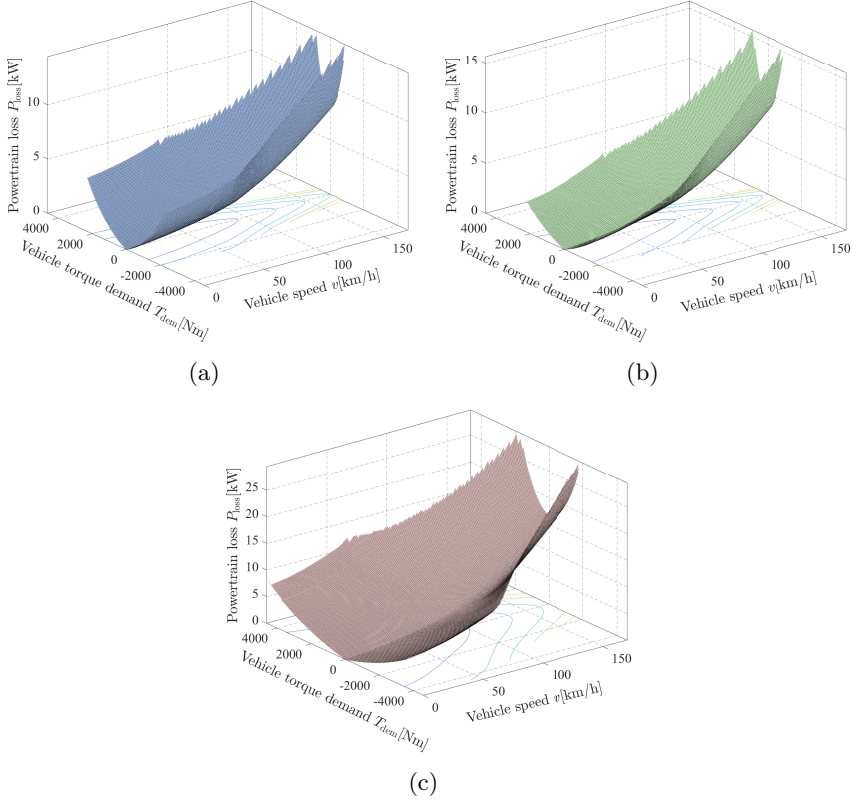


Figure 4.9: *Powertrain losses at different modes: (a) FWD, (b) RWD and (c) AWD.*

The objective function of the DP consists of two terms, powertrain energy losses due to vehicle propulsion and regeneration, and energy losses caused by mode shift transitions. Therefore, the objective function can be formulated as follows:

$$J = \min \sum_{k=0}^{N-1} \Delta T \cdot P_{\text{loss},k}(x, v_k, T_{\text{dem},k}) + E_{\text{shift},k}(x_k, u_k) \quad (4.6)$$

with the constraints of

$$\begin{cases} 1 \leq x_k \leq 3 \\ T_{\min}(x_k, v_k) \leq T_{\text{dem},k} \leq T_{\max}(x_k, v_k) \end{cases} \quad (4.7)$$

where  $P_{\text{loss},k}(x, v_k, T_{\text{dem},k})$  is the powertrain loss at stage  $k$  and  $E_{\text{shift},k}(x_k, u_k)$  is the EDU transient energy loss for a given mode shift command,  $u_k$ , and mode state,  $x_k$ .  $T_{\min}(x_k, v_k)$  and  $T_{\max}(x_k, v_k)$  are the minimum and maximum torque capability of operating mode  $x_k$ .

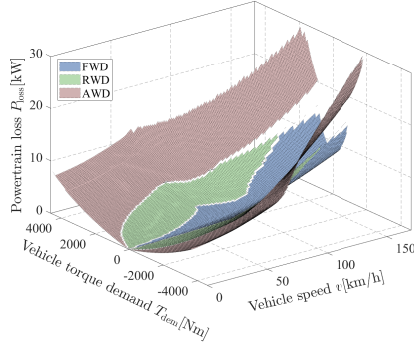


Figure 4.10: *Minimum powertrain loss and corresponding operating mode.*

Given the derived energy-efficient EDU speed control torque trajectories, the corresponding transient energy losses during acceleration from 0 to a target speed and deceleration from a certain speed to 0 can be estimated and stored as a look-up table relative to the target speed and operating speed as shown in Figure 4.11. For convenience, it is mapped in reference to the vehicle speed at which the mode shift and EDU speed control process starts (for example, the vehicle speed to which the EDU must be accelerated and synchronized and the vehicle speed from which EDU is disconnected and decelerated).

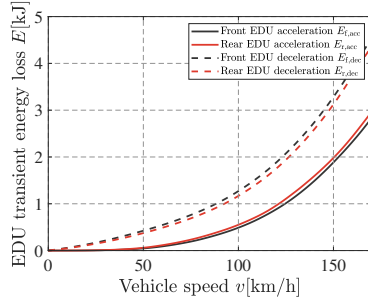


Figure 4.11: *EDU transient energy loss during the speed control process.*

With different operating mode shifts, the transient energy loss,  $E_{\text{shift},k}(u_k)$ , associated with mode shifts is calculated as

$$\begin{cases} E_{1,2} = E_{r,\text{acc}}(v) + E_{f,\text{dec}}(v) \\ E_{2,1} = E_{f,\text{acc}}(v) + E_{r,\text{dec}}(v) \\ E_{1,3} = E_{r,\text{acc}}(v) \\ E_{3,1} = E_{r,\text{dec}}(v) \\ E_{2,3} = E_{f,\text{acc}}(v) \\ E_{3,2} = E_{f,\text{dec}}(v) \end{cases} \quad (4.8)$$

where  $E_{i,j}$  is the transient mode shift energy loss when shifting the powertrain operating mode from mode  $i$  to  $j$ ,  $E_{f/r,\text{acc}}(v)$  is the front or rear EDU energy loss caused by accelerating the EDU speed to match the vehicle speed,  $v$ , and  $E_{f/r,\text{dec}}(v)$  is the front/rear

EDU energy loss caused by decelerating the EDU speed to zero. Both  $E_{f/r,acc}(v)$  and  $E_{f/r,dec}(v)$  are derived in Figure 4.11.

## 4.4 Simulation setup

The simulations are carried out in GT-SUITE environment where the complete vehicle and powertrain system model together with the supervisory controller are implemented as shown in Figure 4.12. The drive cycle is fed as input and the corresponding torque requested by the driver goes into the supervisory controller. Based on the aforementioned control strategies, the final torque demand and clutch command are sent to each EDU and clutch.

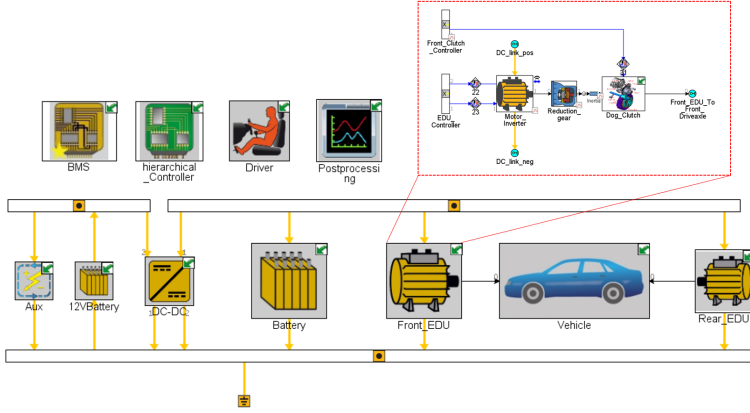


Figure 4.12: *GT-Suite model architecture.*

## 4.5 Results and discussion

The simulations are carried out to calculate the WLTC drive cycle energy consumption of the AFRID powertrain and conventional FRID powertrain. It is worth noting that the conventional FRID powertrain only operates in AWD mode with the optimal torque distribution strategy. In addition, a single motor powertrain is considered as a baseline reference.

### 4.5.1 Transient energy loss

Figure 4.13 illustrates the comparison of instantaneous powertrain power losses between the FRID and AFRID powertrains employing the rule-based mode selection strategy under WLTC drive cycle. The AFRID powertrain predominantly operates in either FWD or RWD mode, activating only one EDU when there is a high torque demand, such as during rapid acceleration events observed in the vehicle start-up phase. This operational

characteristic generally enables the AFRID powertrain to incur lower powertrain losses compared to the FRID powertrain.

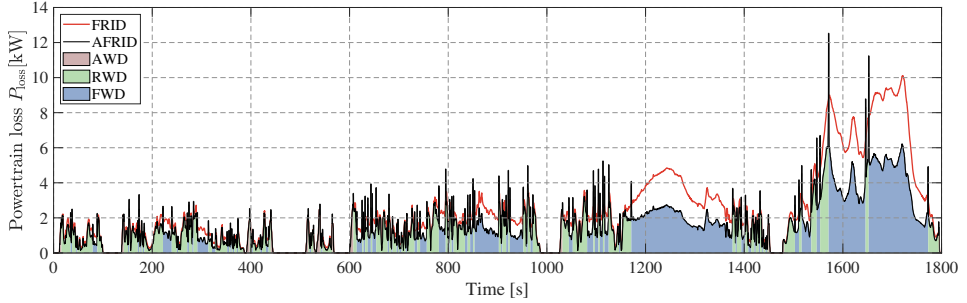


Figure 4.13: *Instantaneous powertrain power losses of FRID powertrain and AFRID powertrain with rule-based mode selection strategy.*

It is also noteworthy that the AFRID powertrain, when operating under the rule-based mode selection strategy, exhibits numerous spikes in instantaneous powertrain power losses during mode transitions. Given the significant variability in driving conditions throughout the WLTC drive cycle, the rule-based mode selection strategy induces frequent mode shifts, resulting in a high frequency of EDU connection and disconnection events. Consequently, the energy losses incurred during these transitions aggregate to a considerable total.

To assess the impact of energy losses during mode shift transitions on overall energy consumption, a baseline scenario is examined. In this scenario, the EDU speed is accelerated and decelerated using maximum and minimum torque, as opposed to employing energy-efficient EDU speed control torque. Table 4.4 presents the comparative results obtained from this analysis. A significant portion of the total powertrain losses can be attributed to the energy losses EDUs experience during mode transitions, accounting for approximately 3% to 4% of the losses. By implementing energy-efficient EDU speed control, the amount of energy loss can be mitigated, leading to a reduction in overall vehicle energy consumption by 0.63%.

Table 4.4: Comparison of max/min torque and energy-efficient EDU speed control.

EDU Speed Control	Energy Cons. [kWh/100km]	Reduction	Transient Loss [kWh/100km]	Overall Loss [kWh/100km]
Max/min torque	20.63	-	0.13	3.19
Energy-efficient	20.50	0.63%	0.10	3.14

#### 4.5.2 Effect of mode selection strategy

Figure 4.14 displays the operating modes derived from both rule-based and DP-based selection strategies for the AFRID powertrain under the WLTC drive cycle. The DP-based

mode selection, informed by future route data, exhibits fewer operating mode shifts and allocates a larger proportion of operation to the AWD mode. Notably, the AWD mode is engaged during deceleration right before each vehicle stop and is maintained for the subsequent vehicle-start acceleration phase. This pattern aligns with expectations, as the AWD mode proves more efficient during vehicle stop-and-start phases where high torque is required at low speeds. Concurrently, the energy losses transiently experienced during the shift to AWD mode are significantly reduced at these low-speed phases.

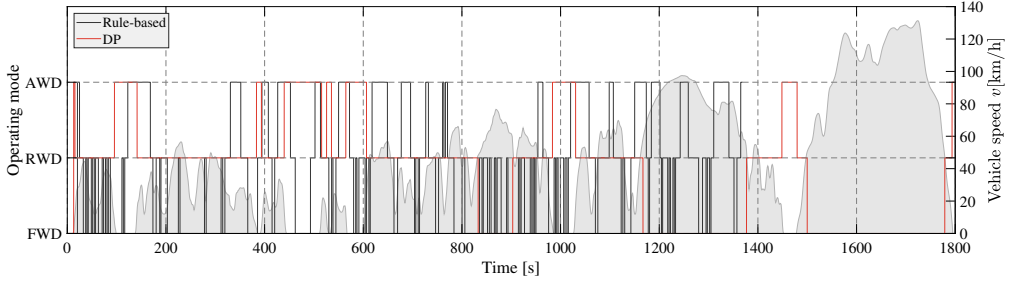


Figure 4.14: *Operating modes derived from rule-based and DP-based selection strategies for the AFRID powertrain under the WLTC drive cycle.*

Table 4.5: Comparison of rule-based and DP mode selection strategy.

Mode Selection Strategy	Energy Cons. [kWh/100km]	Reduction	Number of Mode Shifts	Reduction
Rule-based	20.50	—	143	—
Predictive	20.35	0.73%	23	83.92%

Table 4.5 presents simulation results for the AFRID powertrain employing rule-based and DP-based mode selection strategies. The DP-based mode selection strategy notably reduces the number of mode shifts by 83.92%. This reduction not only alleviates wear on the clutch and associated actuation mechanisms but also diminishes energy consumption. An additional energy savings of 0.73% is observed compared to the rule-based strategy. While the rule-based strategy facilitates transitions to the most energy-efficient mode at any given moment, not every transition necessarily yields energy savings for the powertrain. This is because the energy losses incurred during transitions can offset the benefits. Figure 4.15 provides a detailed illustration of AFRID powertrain instantaneous powertrain power losses with both DP- and rule-based strategies during one small section of the WLTC drive cycle. The rule-based strategy shifts from FWD to RWD and back to FWD. In contrast, the predictive strategy maintains FWD mode throughout this interval. Although the RWD mode results in lower powertrain losses than FWD during this period, the energy saved is outweighed by the additional transient losses from mode shifts. In this case, the rule-based strategy leads to decreased energy efficiency due to increased mode shifts. However, the DP-based strategy, informed by pre-known route data, avoids unnecessary shifts. By carefully weighing the benefits of operating in the

most energy-efficient mode against the transient losses from shifts, the DP-based mode selection strategy further optimizes the energy consumption of the AFRID powertrain.

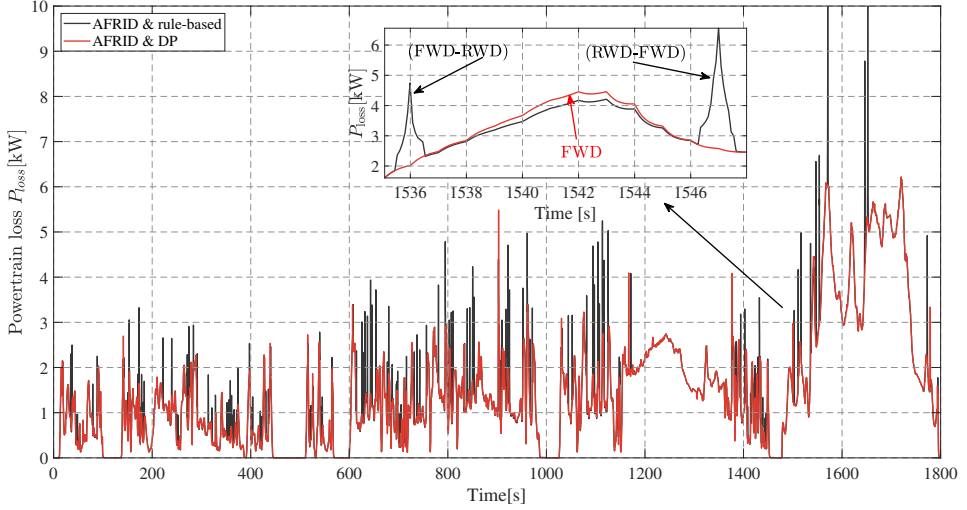


Figure 4.15: *Instantaneous powertrain power losses of AFRID with DP- and rule-based mode selection strategy during the WLTC drive cycle between 1536s and 1548s.*

### 4.5.3 Energy efficiency improvement

The energy consumption results of FRID, AFRID and single motor powertrain under WLTC cycle are summarized in Table 4.6. Firstly, it is observed that the energy consumption of the FRID powertrain is 7.71% higher in comparison to the single motor powertrain. Nonetheless, with the help of the clutches and disconnect functionality of the AFRID powertrain, the decreased energy efficiency of the dual motor powertrain can be almost fully mitigated while maintaining the advantages of FRID powertrains. As a result, the AFRID powertrain achieves a significant energy consumption reduction of 8.21% compared to the FRID powertrain and shows slightly lower energy consumption compared to the single motor powertrain.

Table 4.6: Energy consumption of FRID, AFRID and single motor powertrain under WLTC drive cycle.

Powertrain	Energy cons. [kWh/100km]	Reduction
FRID	22.17	—
AFRID	20.35	8.21%
Single motor *	20.46	7.71%

\*EDU with stranded winding PMSM and vehicle weight deviation is not included.

# 5 Adjustable DC-Link Voltage Powertrain

In a conventional BEV powertrain as discussed in Section 1.2, fluctuations in the DC-link voltage stemming from the battery's dynamic behaviors like variations in SoC and voltage drops can lead to a deterioration of the powertrain's energy efficiency and performance [85]. For PMSMs, the widely utilized maximum-torque-per-ampere (MTPA) control strategy enables the delivery of specific torque at a certain speed while minimizing current usage, which in turn cuts down on copper loss in the motor. This strategy, however, is constrained by the DC voltage supply  $V_{dc}$ . The resulting maximum peak phase voltage  $v_{s,max}$  is represented as an ellipse as illustrated in Figure 5.1. In the d- and q-axis current ( $i_d - i_q$ ) plane, the voltage limit is described as:

$$\frac{(i_d + \frac{\Psi_m}{L_d})^2}{L_q^2} + \frac{i_q^2}{L_q^2} \leq (\frac{v_{s,max}}{\omega_r L_d L_q})^2 \quad (5.1)$$

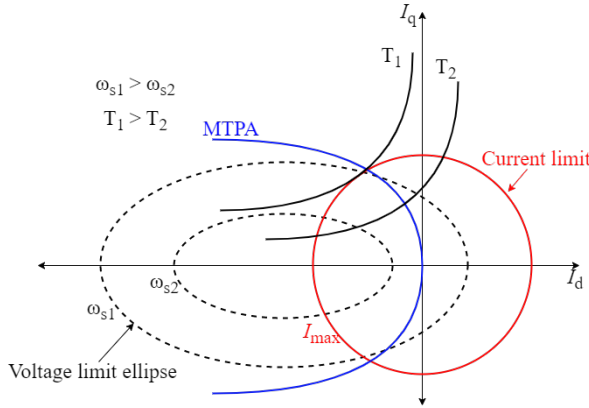


Figure 5.1: *Illustration of maximum-torque-per-ampere (MTPA) control strategy.*

The corresponding speed, also denoted as base speed ( $\omega_s$ ), marks the highest speed at which the motor can maintain the MTPA strategy and adhere to the voltage constraint. When operating beyond the base speed, the field weakening strategy is employed by injecting negative  $i_d$  to reduce rotor flux. This allows for extending motor operational speeds preventing motor back EMF from damaging the electrical system but results in increased motor losses and reduced torque output, as the motor operates outside its optimal MTPA range.

Figure 5.2 illustrates the loss maps of a PMSM with different DC voltage inputs. Below the base speed (prior to DC voltage saturation), the PMSM's loss and torque output are relatively unaffected by the DC-link voltage due to the MTPA strategy. As the DC

voltage increases, the MTPA operating range extends (with a corresponding increase in base speed), enhancing torque output and efficiency at higher operating speeds.

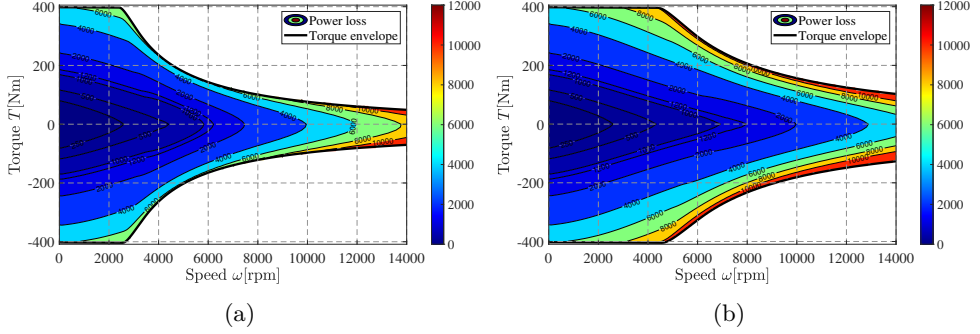


Figure 5.2: *PMSM loss maps: (a) with 250 V DC voltage and (b) with 450 V DC voltage.*

On the other hand, the inverter loss is also affected by DC-link voltage. Figure 5.3 depicts the inverter loss maps with various DC voltages supplied. Lower DC-link voltage proves advantageous for efficiency at low speeds. When operating under the MTPA strategy below base speed, the current required is consistent across different DC voltages, leading to identical conduction losses within the inverter. However, lower DC voltage results in reduced switching loss hence lowered inverter loss. At higher speeds, conduction loss becomes the predominant factor in inverter loss. Since higher DC voltage extends the motor's MTPA operation, the current requirement decreases, leading to reduced inverter loss.

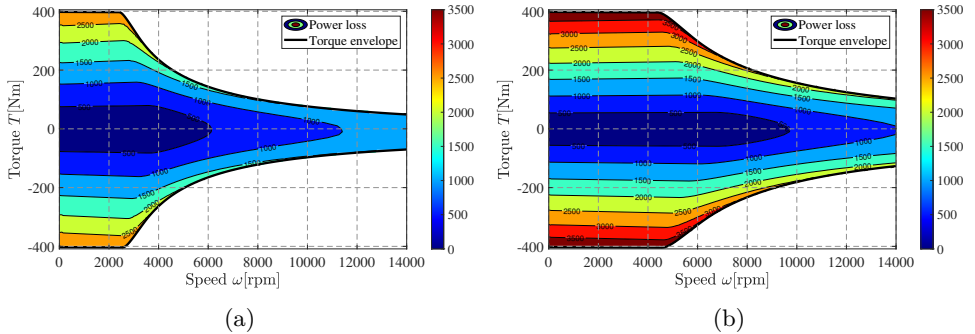


Figure 5.3: *Inverter loss maps (Infineon FS820R08A6P2B): (a) with 250 V DC voltage and (b) with 450 V DC voltage.*

Therefore, depending on vehicle operation conditions, different DC voltage supplied is favored. However, it is impractical to design a conventional BEV powertrain's battery pack that can adapt its DC voltage to accommodate all driving conditions optimally.



To further optimize the powertrain efficiency and performance, an additional DC-DC converter can be introduced to decouple the battery from the DC and dynamically adjust DC-link voltage according to different driving conditions

## 5.1 Powertrain configuration

The adjustable DC-link voltage powertrain configuration powertrain, as illustrated in Figure 5.4, features a bidirectional boost DC-DC converter as already illustrated in Section 3.4.1. This setup enables boost operation from the battery terminal to the DC-link and buck operation from the inverter to the battery terminal, corresponding to the propulsion and regeneration modes, respectively.

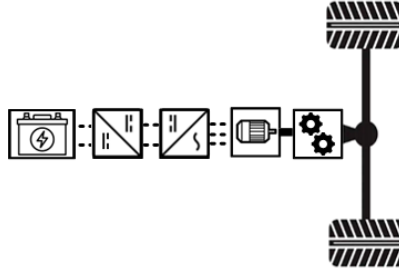


Figure 5.4: *Adjustable DC-link voltage powertrain configuration with bidirectional DC-DC converter.*

For the DC-DC converter and inverter, both IGBT and MOSFET transistors are examined in this study. The selected IGBT power module is the FS820R08A6P2B from Infineon. In comparison to IGBTs, MOSFETs possess a lower current handling capability due to the current state of MOSFET wafer process technology and the absence of large die sizes capable of supporting high current capacities [86]. To address this, the study employs two parallel-connected CREE SiC MOSFET CAS300M12BM2 (300A 1200V) half-bridge modules for each leg, ensuring a current rating equivalent to that of the FS820R08A6P2B (820A 750V). This configuration is designed to accommodate the powertrain's worst operating points.

## 5.2 Powertrain operation strategy

To thoroughly optimize powertrain efficiency across various driving conditions through DC-link voltage adjustments, it is imperative to account for losses throughout the entire powertrain. This includes additional losses incurred by the DC-DC converter and the effects of variations in battery voltage.

### 5.2.1 DC-link voltage operating boundary

In the adjustable DC-link voltage powertrain, the DC-link voltage serves as a degree of freedom to be controlled. Nevertheless, the selected DC-link voltage must align with the specifications of other powertrain components, necessitating the establishment of upper and lower operating boundaries for the DC-link voltage.

The blocking voltage for the selected IGBT pack is 750 V. To safeguard the power module from potential damage due to voltage spikes during switching events, a safety margin is implemented, setting the upper operational boundary for the DC-link voltage at 450 V in the IGBT-based powertrain. On the other hand, while the MOSFET module can withstand a voltage of 1200 V that is significantly higher than the IGBT. This study aims for a generalized comparison of energy efficiency gains in the powertrain due to the MOSFET's low-loss feature, without accentuating the substantial loss reduction in the PMSM by elevating the DC-link voltage to excessively high levels, which might induce insulation problems in the motor winding. Hence, the upper operational boundary for the DC-link voltage in the MOSFET-based powertrain is also set at 450 V, aligning with the IGBT-based counterpart. For the lower boundary, the scenario where the battery is at its minimum SoC, 10 %, is considered as the worst case, corresponding to an open circuit voltage of 280 V (refer to Figure 3.8a). In case of high power demand such as full-throttle acceleration, a voltage drop of 10 % might occur due to internal resistance, bringing the lowest DC-link voltage down to 250 V. Therefore, the DC-link voltage operational range is defined as spanning from 250 V to 450 V.

### 5.2.2 DC-link voltage selection strategy

To explore the full potential of energy efficiency improvements offered by adjustable DC-link voltage, DP is employed to determine the optimal DC-link voltage sequence, taking into account the overall powertrain loss, particularly the additional loss introduced by the DC-DC converter.

The battery SoC is chosen as the only state variable  $x$ , ranging between 5% and 95%. The DC-link voltage ( $V_{dc}$ ) is defined as the control variable  $u$  which stays within the operating boundary defined previously. At each stage of the discretized time span over the drive cycle, the propagation of state is expressed as:

$$x_{k+1} = -\frac{I_{bat,k}(x_k, u_k)}{Q_c} \Delta T + x_k, \quad k = 0, 1, \dots, N-1 \quad (5.2)$$

where  $Q_c$  is the battery capacity. The objective function of the DP, representing the accumulated overall powertrain losses, can then be described as:

$$J = \min \sum_{k=0}^{N-1} [P_{bat,loss}(u_k, x_k) + P_{inv,loss}(u_k, \omega, T) + P_{motor,loss}(u_k, \omega, T) + P_{DCDC,loss}(u_k, x_k)] \Delta T \quad (5.3)$$

with the constraints of

$$\begin{aligned}
0.05 &\leq \text{SoC} \leq 0.95 \\
T_{\min}(\omega, V_{\text{dc}}) &\leq T \leq T_{\max}(\omega, V_{\text{dc}}) \\
V_{\text{bat}} &\leq V_{\text{dc}} \leq 450 \text{ V} \\
-820 \text{ A} &\leq I_{\text{bat}} \leq 820 \text{ A}
\end{aligned} \tag{5.4}$$

The powertrain losses under consideration include battery loss ( $P_{\text{bat,loss}}$ ), DC-DC converter loss ( $P_{\text{DCDC,loss}}$ ), inverter loss ( $P_{\text{inv,loss}}$ ), and motor loss ( $P_{\text{motor,loss}}$ ). Losses in the motor and inverter are calculated based on the motor's operating speed and torque given a specified DC-link voltage  $V_{\text{dc}}$ . However, the DC-DC converter and battery losses are dependent on the battery's current and terminal voltage, which are affected by the DC-DC converter loss in return. Therefore, to estimate the losses in the battery and converter accurately, it is essential to calculate the battery current initially. This calculation is based on the power balance at the DC-link, as follows:

$$P_{\text{bat}} - P_{\text{DCDC,loss}} = P_{\text{inv,loss}} + P_{\text{motor,loss}} + P_{\text{mech}} \tag{5.5}$$

where  $P_{\text{bat}}$  is the battery terminal power and  $P_{\text{mech}}$  is the mechanical power of the motor.

For convenience, the right-hand side of (5.5) can be denoted as DC-link power demand  $P_{\text{dc}}$ :

$$P_{\text{dc}}(V_{\text{dc}}, \omega, T) = P_{\text{inv,loss}}(V_{\text{dc}}, \omega, T) + P_{\text{motor,loss}}(V_{\text{dc}}, \omega, T) + P_{\text{mech}}(\omega, T) \tag{5.6}$$

Since the operating points for a normal drive cycle are far below the nominal power rating of the inverter, the junction temperatures of the transistors and diodes change only slightly over the drive cycle. Thus, for simplicity, the effect of temperature variation on the losses is omitted in the analytical loss model of the inverter as well as the DC-DC converter described in Section 3.4.1 and Section 3.4.2, and the parameters used for transistors and diodes are obtained at a junction temperature of  $65^\circ\text{C}$  in correspondent to the normal working temperature in a real vehicle. For the chosen power modules, the IGBT power module has the  $K_{it}$  value of 1,  $K_{vt}$  value of 1.3,  $K_{id}$  value of 1, and  $K_{vd}$  value of 0.6 and the MOSFET power module has the  $K_{it}$  value of 1 and a  $K_{vt}$  value of 1.4. By combining Equations (3.14), (3.15), (3.17), (3.18), (3.19), (3.8), (3.7), (3.6), (5.5), and (5.6), the battery current can be derived as a feasible root of a cubic polynomial equation for an IGBT-based powertrain as:

$$aI_{\text{bat}}^3 + bI_{\text{bat}}^2 + cI_{\text{bat}} + d = 0 \tag{5.7}$$

and a feasible root of a quadratic equation for a MOSFET-based powertrain as:

$$bI_{\text{bat}}^2 + cI_{\text{bat}} + d = 0 \tag{5.8}$$

where  $a$ ,  $b$ ,  $c$  and  $d$  are the coefficients for the polynomial equations listed in Table 6.1 in the Appendix. This formulation allows for the determination of the battery current, hence the corresponding DC-DC converter loss under various operating conditions and battery states during the DP process.

### 5.3 Simulation setup

A comprehensive vehicle and powertrain model, incorporating detailed power electronics loss models and control, has been developed in the PLECS and Simulink environment. Figure 5.5 illustrates the control structure. The derived DC-link voltage from the DC-link voltage selection strategy, denoted as  $V_{dc}^*$  and highlighted with a turquoise line, is fed to both the DC-DC converter controller and the PMSM's field-oriented current controller. The field-oriented current control scheme, which includes active damping (enclosed by a dashed green box) and anti-windup (also enclosed by a dashed green box), is delineated with blue lines. For details on the parameterization of control parameters, including the gains of the PI controller, refer to [87]. Mechanical system quantities, such as vehicle speed, are indicated with orange lines.

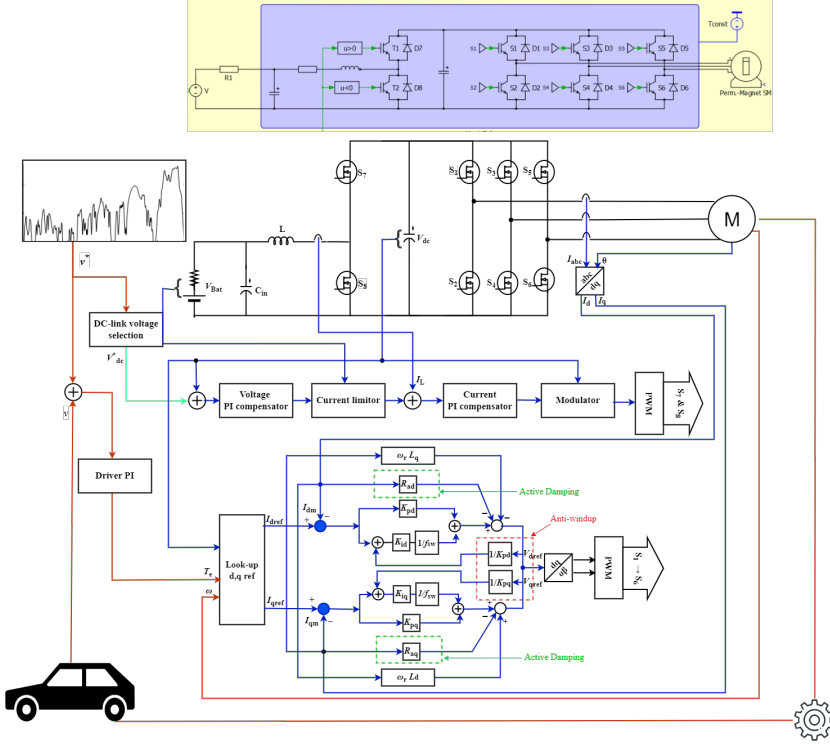


Figure 5.5: Schematic illustration of the inverter/PMSM and DC-DC converter control for the adjustable DC-link voltage powertrain.

### 5.4 Results and discussion

The simulations are carried out to calculate the WLTC drive cycle energy consumption of the adjustable DC-link powertrain and the conventional powertrain without the flexibility

to adapt the DC-link voltage as the baseline. Consequently, four distinct topologies are examined: (1) Baseline powertrain with an IGBT-based inverter, (2) adjustable DC-link voltage powertrain with IGBT-based DC-DC converter and inverter, (3) baseline powertrain with a MOSFET-based inverter, and (4) adjustable DC-link voltage powertrain with MOSFET-based DC-DC converter and inverter. To assess the impact of battery terminal voltage deviations resulting from different states of charge (SoC) on powertrain energy efficiency, initial battery SoC values of 20 % and 80 % are investigated, representing low and high SoC scenarios. Furthermore, the result of improvement in the vehicle acceleration performance is also presented.

#### 5.4.1 Optimized DC-link voltage

The optimized DC-link voltage for the adjustable DC-link voltage powertrain derived from DP calculation and the DC-link voltage (battery terminal voltage) for the baseline powertrain are depicted in Figure 5.6.

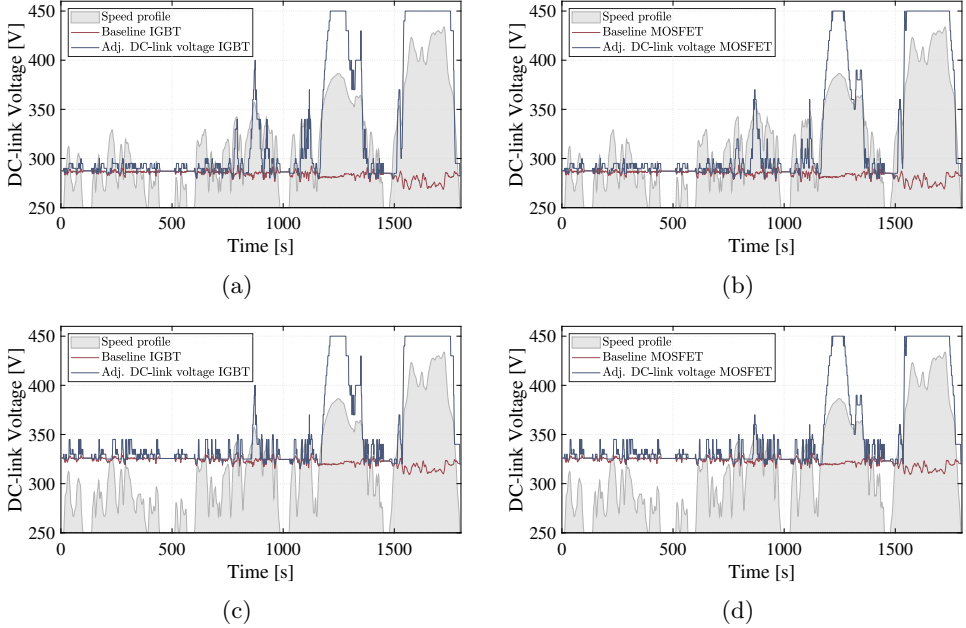


Figure 5.6: *Optimized DC-link voltage in adjustable DC-link voltage powertrain compared with DC-link voltage in baseline powertrain: (a) IGBT-based powertrains with low battery SoC, (b) MOSFET-based powertrains with low battery SoC, (c) IGBT-based powertrains with high battery SoC and (d) MOSFET-based powertrains with high battery SoC.*

In all four cases examined, it is noted that the optimal DC-link voltage for the adjustable DC-link voltage powertrain predominantly stays low, aligning closely with the battery terminal voltage under low-speed conditions. While during operations at high and

extra-high speeds, the optimal DC-link voltage for both IGBT and MOSFET-based adjustable DC-link voltage powertrains tends to approach the upper limit. On the other hand, in medium-speed operation scenarios, the switching losses within the power electronics are of a magnitude comparable to the conduction losses present in both the power electronics and the motor. As a result, the IGBT-based adjustable DC-link powertrain and the MOSFET-based counterpart exhibit divergent optimal DC-link voltages. This discrepancy is due to the varying trade-offs among the different types of losses, which are significantly influenced by the specific characteristics of the selected MOSFETs and IGBTs.

### 5.4.2 Energy efficiency improvement

The drive cycle energy consumption results for the four cases are listed in Table 5.1. Leaving the adjustable DC-link voltage powertrain aside, merely incorporating MOSFETs into baseline powertrains yields a substantial reduction in energy consumption over the WLTC cycle, approximately 2.8 % for both low and high battery SoC levels. As documented in [6, 64], inverters with MOSFETs, on average, exhibit losses that are three times lower than IGBTs-based counterparts, underscoring the low-loss advantage inherent to MOSFETs.

Table 5.1: Energy consumption of baseline and adjustable DC-link voltage powertrain under WLTC drive cycle.

Init. SoC	Powertrain	Energy cons. [kWh/100km]	Reduction
20%	Baseline powertrain IGBT	20.28	-
	Adj. DC-link voltage powertrain IGBT	19.77	2.51%
20%	Baseline powertrain MOSFET	19.72	-
	Adj. DC-link voltage powertrain MOSFET	19.08	3.25%
80%	Baseline IGBT	19.85	-
	Adj. DC-link voltage powertrain IGBT	19.62	1.16%
80%	Baseline MOSFET	19.29	-
	Adj. DC-link voltage powertrain MOSFET	18.92	1.92%

Concerning the influence of battery SoC, a decline from 80 % to 20 % results in a reduction of energy consumption by approximately 2.1 % for both IGBT-based and MOSFET-based baseline powertrains. Nevertheless, the efficiency degradation associated with varying battery SoC levels is alleviated with the implementation of adjustable DC-link voltage powertrains. The percentage of efficiency deterioration is reduced to about 0.8 % in the case of adjustable DC-link voltage powertrains, rendering the powertrain efficiency less susceptible to changes in battery SoC. This observation suggests an additional benefit of adjustable DC-link voltage powertrains: they can sustain consistent energy efficiency levels irrespective of the battery SoC, unlike their baseline counterparts.

At low battery SoC levels, IGBT-based powertrains experience a 2.51 % reduction in energy consumption with the adjustable DC-link voltage. This reduction in energy consumption is further amplified to 3.25 % in the case of MOSFET-based powertrains. For high battery SoC levels, the observed trend is consistent. However, the efficiency improvement with adjustable DC-link voltage is marginally smaller compared to scenarios with low battery SoC levels. This diminished improvement is attributed to the fact that baseline powertrains with high battery SoC inherently exhibit enhanced powertrain efficiency in medium and high-speed sections in the WLTC drive cycle. Despite these factors, powertrains with adjustable DC-link voltage continue to offer noteworthy reductions in energy consumption relative to baseline powertrains, with efficiency gains ranging from 1.16 % to 1.92 % for IGBT and MOSFET-based powertrains, respectively.

Figure 5.7 summarizes the individual powertrain component losses. It is noticeable that battery losses are similar across cases within the same battery SoC levels. However, a higher battery SoC yields lower ohmic losses within the battery. When comparing the baseline powertrain with the adjustable DC-link voltage powertrain, the primary source of loss reduction lies in motor losses and a minor decrease in inverter losses. This improvement compensates for the additional losses incurred by the DC-DC converter. Nevertheless, in the IGBT-based adjustable DC-link voltage powertrain, the extra losses from the DC-DC converter still represent a substantial portion of the total powertrain losses. Conversely, employing MOSFETs in the adjustable DC-link powertrain not only achieves the enhanced motor efficiency observed in the IGBT-based counterpart but also incurs significantly lower losses in the power electronics, making the additional DC-DC converter loss almost negligible and maximizing the energy-saving potential of the adjustable DC-link voltage powertrain.

### 5.4.3 Vehicle performance improvement

Another significant advantage of utilizing an adjustable DC-link voltage is its capability to extend the range of constant torque operation through the elevation of the DC-link voltage. In scenarios where there is a demand for full-load acceleration (e.g., 0 - 100 km/h test), the DC-link voltage is strategically boosted to ensure the maximization of torque output relative to the increased vehicle speed.

Table 5.2 presents the time required to accelerate the vehicle from standstill to 100 km/h, taking into account the effect of tire slip. It is important to highlight that the discussion focuses on IGBT-based powertrains, as the performance differences between MOSFET-based and IGBT-based powertrains are negligible.

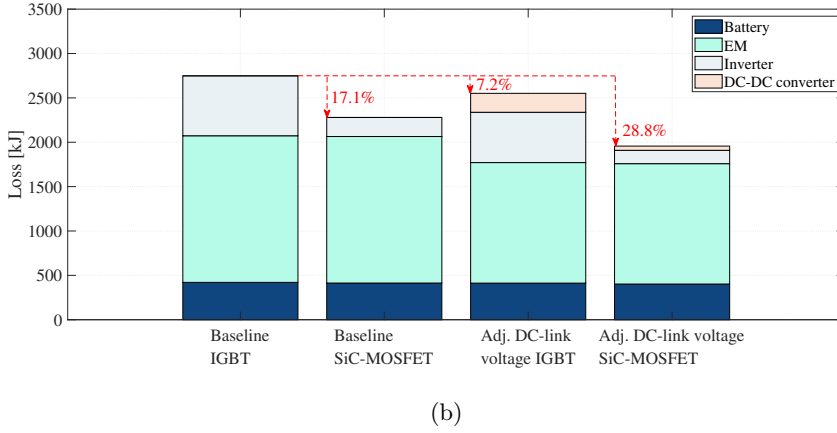
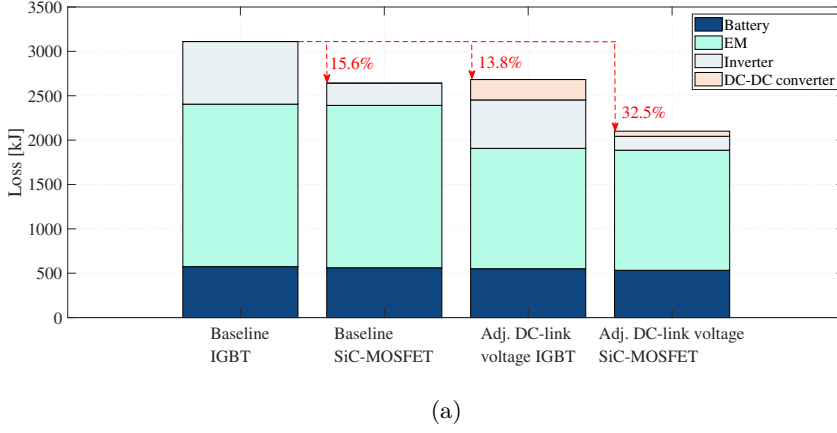


Figure 5.7: Powertrain losses breakdown under WLTC drive cycle: (a) low battery SoC and (b) high battery SoC.

Table 5.2: 0 - 100 km/h acceleration time simulation results.

Init. SoC	Powertrain	Time [s]
20%	Baseline	13.4
	Adj. DC-link voltage	8.4
80%	Baseline	11.8
	Adj. DC-link voltage	8.4

The results demonstrate that the baseline BEV powertrain experiences a decline in acceleration performance as the battery SoC level decreases. Specifically, a deterioration of 1.6 seconds is witnessed when the battery SoC drops from 80% to 20%. This performance degradation is attributable to the diminished DC-link voltage (i.e., battery terminal voltage) supplied to the inverter, as shown in Figure 5.8a. Furthermore, during full



load conditions, the battery experiences approximately a 10% voltage drop across its internal resistance due to high current flow. This voltage drop further exacerbates the performance deterioration observed in the baseline BEV powertrain. In contrast, with the help of a DC-DC converter, the DC-link voltage can be maintained at a predetermined value, unaffected by the battery's dynamics in the adjustable DC-link voltage powertrain, resulting in up to 5 seconds faster acceleration time. Hence, the adjustable DC-link voltage powertrain exhibits consistent superior acceleration performance and torque output regardless of the battery SoC level (as depicted in Figure 5.8b).

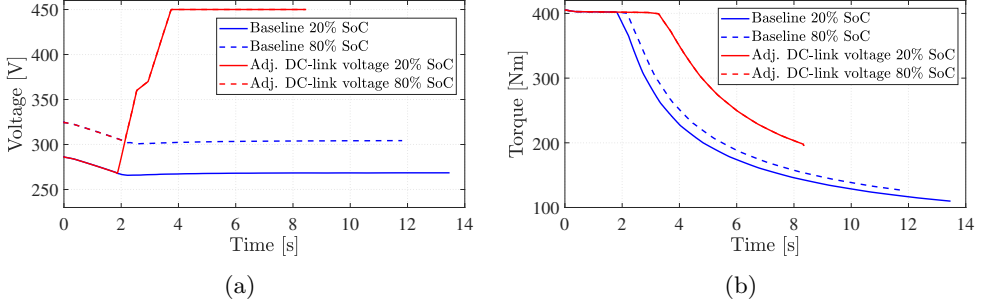


Figure 5.8: Results of 0 - 100 km/h acceleration: (a) DC-link voltage and (b) motor torque output.



# 6 Conclusion and Future Work

## 6.1 Conclusion and Discussion

In this thesis, the energy efficiency improvement of two novel powertrain topologies, the AFRID powertrain and the adjustable DC-link voltage powertrain, has been systematically investigated through simulation-based methodologies.

The AFRID powertrain, characterized by its unique disconnect functionality due to the incorporation of dog clutches, demonstrated significant potential for enhancing energy efficiency. The introduction of the clutches between the EDU and the drive axle effectively mitigated the no-load losses in EDUs. The implementation of the DP-based optimization mode strategy, supported by predictive route information, further reduces the energy consumption of the AFRID powertrain by balancing the benefits of the flexibility of various powertrain operating modes against the transient losses incurred during mode shifts, culminating in an 8.21% reduction in energy consumption and a significant decrease in clutch actuations under the WLTC drive cycle compared to conventional FRID powertrain. In other words, the AFRID powertrain addresses the inherent high no-load loss issue found in conventional FRID powertrains without disconnect functionality while maintaining the advantages of FRID powertrains, such as fault-tolerance, all-wheel-drive, and torque distribution capability.

Furthermore, the findings indicate that AFRID powertrains could theoretically achieve greater energy efficiency than conventional single motor powertrains, assuming the weight difference is disregarded. The more distinct the high-efficiency zones are for the front and rear EDUs at both low and high speeds, the greater the efficiency enhancement possible with AFRID powertrains. However, when considering the additional weight of a second EDU, the extent of energy efficiency improvement over single motor powertrains may vary, depending on the specific weight of the EDU and vehicle attributes.

Nevertheless, adding additional mechanical clutches can introduce challenges in mechanism control and incur extra costs. In the current BEV market, manufacturers have become aware of powertrain efficiency deterioration due to high no-load losses in PMSM-based EDUs. For example, the Kia E-GMP Platform has introduced a single clutch to disconnect one of the EDUs when it's not needed, representing a reasonable trade-off for cost-effectiveness. However, for two PMSMs optimized for different driving conditions, a single clutch is insufficient to fully utilize the high-efficiency characteristics of each EDU. Furthermore, the study presented strictly follows the specified driving cycle, so the free-coasting mode with both front and rear clutches disconnected is not discussed. In real-world driving, this mode could be utilized for free-coasting when deviation from the speed profile is permitted, similar to adaptive cruise control, potentially pushing the energy efficiency of AFRID powertrains with two clutches to further boundaries. On the other hand, pairing a PMSM with a different type of electric motor, such as an IM —

known for its low no-load loss and complimentary high efficiency in contrast to PMSM, could be an equally viable cost-effective solution with a simpler structure and easier control.

The adjustable DC-link voltage powertrain, integrated with a DC-DC boost converter, facilitates dynamic adjustment of the DC-link voltage in response to varying powertrain operating conditions. The DP-optimized DC-link voltage control strategy, which considers variations in battery terminal voltage, enhances the energy efficiency of the adjustable DC-link voltage powertrain compared to conventional counterparts where the DC-link is directly coupled with the battery. This results in energy consumption reductions of up to 2.51% for IGBT-based systems and 3.25% for MOSFET-based systems under the WLTC drive cycle as incorporation of MOSFETs further amplifies the energy-saving potential of adjustable DC-link voltage powertrains. Additionally, the adjustable DC-link voltage powertrain mitigates the energy efficiency and vehicle performance deterioration observed in conventional powertrains by decoupling the battery and DC-link voltage.

The presented results suggest that the effectiveness of adjustable DC-link voltage powertrains in enhancing energy efficiency is case-specific, depending on factors such as the battery pack voltage, vehicle attributes and driving conditions. This study focuses on a particular instance involving a 300 V battery system with a boost DC-DC converter. However, with the growing trend towards faster battery charging, battery packs are shifting from 300 - 400 V to 800 V or even more. As demonstrated in BorgWarner's findings (see Figure 6.1 ), in a comprehensive driving cycle encompassing both low and high-speed scenarios, a conventional powertrain with a higher system voltage may lead to higher energy consumption. This increased consumption can potentially be offset in an adjustable DC-link voltage powertrain equipped with a DC-DC buck converter.

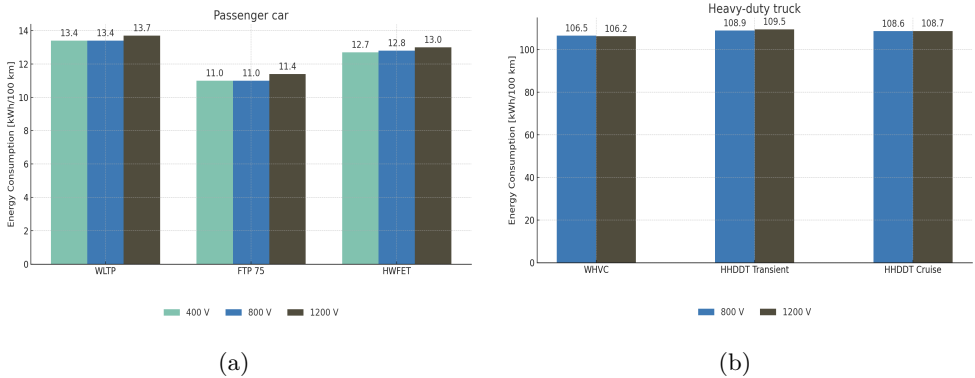


Figure 6.1: Comparison of energy consumption for different drive cycles and different system voltages: (a) passenger car and (b) heavy-duty truck. [88]

Nevertheless, the efficiency gains from adjustable DC-link voltage powertrains are relatively minor when using a high-voltage battery with a buck converter, compared to

a low-voltage battery with a boost converter. This is because, in high-voltage setups, energy savings mainly arise from reduced inverter losses at lower speeds. In contrast, low-voltage setups can reduce both inverter and motor losses at higher speeds, where the absolute reduction in losses is more substantial than the savings at lower speeds. Therefore, adjustable DC-link voltage powertrains are more effective with low-voltage batteries and boost converters, especially when fast charging is not a priority.

In addition, the additional losses and costs associated with DC-DC converters could potentially hinder their adoption. The study points out that employing low-loss switches, such as MOSFETs, could lessen these additional losses, but this comes at a greater expense. However, high-voltage gallium nitride (GaN) devices, a newly emerging WBG material, are swiftly gaining market traction [89]. These devices offer notable benefits like enhanced energy efficiency, compactness, reduced weight and lower costs. This makes them a potentially promising alternative to improve the overall cost-effectiveness of adjustable DC-link voltage powertrains.

For the two studied powertrain topologies, DP has been used to identify the globally optimal control strategy, thereby evaluating the maximum potential for powertrain energy efficiency improvement. On one hand, this approach can be used to calibrate rule-based strategies for real-world applications. This is particularly relevant in the context of fleet and public transportation, where routes are known and repeated daily. On the other hand, for applications like autonomous vehicles or those using GPS-based near-future route information, DP can be executed online to determine an optimized control strategy over a shorter time horizon while the vehicle is in operation with speed information being continuously updated.

The integration of the investigated novel powertrain topologies with state-of-the-art components promises substantial improvements in powertrain energy efficiency. Vehicles that incorporate these powertrains are predicted to showcase lower energy consumption and possibly better performance and drivability. The insights gained from this thesis contribute meaningful understanding to the realm of sustainable transportation which is foreseen to shape the development endeavors in the design of BEV powertrains.

## 6.2 Future work

The current study does not account for the temperature dependency of powertrain components' loss models. Future research endeavors should incorporate temperature dependency into powertrain loss assessments and consider powertrain cooling control as an additional degree of freedom in optimizing energy efficiency. This necessitates the development of detailed thermal modeling for each component, temperature-dependent loss assessments, and a comprehensive thermal system for the electric powertrain, providing a more accurate and holistic understanding of the system's thermal dynamics and efficiency.

Secondly, the study so far has primarily focused on hardware-based design optimization for the powertrain, which inevitably incurs additional costs due to the need for extra components and reliance on advanced, state-of-the-art components. To mitigate these expenses, it would be beneficial to explore software-based optimization strategies. Future work in this area should investigate innovative electric drive control strategies, offering a potentially cost-effective approach to enhancing powertrain efficiency without resorting to hardware modifications or additions.

Lastly, the possibilities should be sought to supplement the simulation-based approach of this thesis with testing to validate the results. This could involve exploring options like Hardware-in-the-Loop (HIL) simulations for a more controlled testing environment and possibly conducting comprehensive vehicle tests to evaluate the performance of the systems in real-world conditions.

# Bibliography

- [1] Yanmei Li, Ningning Ha, and Tingting Li. “Research on carbon emissions of electric vehicles throughout the life cycle assessment taking into vehicle weight and grid mix composition”. In: *Energies* 12.19 (2019), p. 3612.
- [2] Johannes Buberger, Anton Kersten, Manuel Kuder, Richard Eckerle, Thomas Weyh, and Torbjörn Thiringer. “Total CO<sub>2</sub>-equivalent life-cycle emissions from commercially available passenger cars”. In: *Renewable and Sustainable Energy Reviews* 159 (2022), p. 112158.
- [3] Paweł Bryła, Shuvam Chatterjee, and Beata Ciabiada-Bryła. “Consumer adoption of electric vehicles: A systematic literature review”. In: *Energies* 16.1 (2022), p. 205.
- [4] Vinodkumar Etacheri, Rotem Marom, Ran Elazari, Gregory Salitra, and Doron Aurbach. “Challenges in the development of advanced Li-ion batteries: a review”. In: *Energy & Environmental Science* 4.9 (2011), pp. 3243–3262.
- [5] IEA. *Electric car registrations and sales share in China, United States and Europe, 2018-2022*. Licence: CC BY 4.0. IEA. 2022. URL: <https://www.iea.org/data-and-statistics/charts/electric-car-registrations-and-sales-share-in-china-united-states-and-europe-2018-2022>.
- [6] Alexander Nisch, Christian Klöffler, Jörg Weigold, Wolfgang Wondrak, Christian Schweikert, and Laurent Beaurenaud. “Effects of a SiC TMOSFET tractions inverters on the electric vehicle drivetrain”. In: *PCIM Europe 2018; International Exhibition and Conference for Power Electronics, Intelligent Motion, Renewable Energy and Energy Management*. VDE. 2018, pp. 1–8.
- [7] Sepideh Amirpour, Torbjörn Thiringer, and Dan Hagstedt. “Power loss analysis in a SiC/IGBT propulsion inverter including blanking time, MOSFET’s reverse conduction and the effect of thermal feedback using a PMSM model”. In: *IECON 2020 The 46th Annual Conference of the IEEE Industrial Electronics Society*. IEEE. 2020, pp. 1424–1430.
- [8] T Dimier, M Cossale, and T Wellerdieck. “Comparison of stator winding technologies for high-speed motors in electric propulsion systems”. In: *2020 International Conference on Electrical Machines (ICEM)*. Vol. 1. IEEE. 2020, pp. 2406–2412.
- [9] Grazia Berardi, Shafigh Nategh, Nicola Bianchi, and Yves Thiolier. “A comparison between random and hairpin winding in e-mobility applications”. In: *IECON 2020 The 46th Annual Conference of the IEEE Industrial Electronics Society*. IEEE. 2020, pp. 815–820.

- [10] William Cai, Xiaogang Wu, Minghao Zhou, Yafei Liang, and Yujin Wang. “Review and development of electric motor systems and electric powertrains for new energy vehicles”. In: *Automotive Innovation* 4 (2021), pp. 3–22.
- [11] B Wex, B Pötzelberger, W Gruber, and S Silber. “Performance Comparison between Hairpin and Round Wire Winding for a 17,000 rpm PMSM”. In: *2022 International Conference on Electrical Machines (ICEM)*. IEEE. 2022, pp. 1662–1668.
- [12] Raj Shah, Blerim Gashi, and Andreas Rosenkranz. “Latest developments in designing advanced lubricants and greases for electric vehicles—An overview”. In: *Lubrication Science* 34.8 (2022), pp. 515–526.
- [13] Monica Beyer, Gareth Brown, Michael Gahagan, Tomoya Higuchi, Gregory Hunt, Michael Huston, Doug Jayne, Chris McFadden, Timothy Newcomb, Suzanne Patterson, et al. “Lubricant concepts for electrified vehicle transmissions and axles”. In: *Tribology Online* 14.5 (2019), pp. 428–437.
- [14] Lawrence Alger, James Haybittle, Anthony D Wearing, Cedric Rouaud, and William D Drury. “A 25 kW 48 V Mild Hybrid Motor and Inverter: Development of High-Power, 6-Phase, Frameless 48 V IPM Motor and an Oil-Cooled Inverter with Low Thermal Resistance”. In: *CTI SYMPOSIUM 2018: 17th International Congress and Expo 3-6 December 2018, Berlin, Germany*. Springer. 2020, pp. 1–19.
- [15] Xibo Yuan and Jiabin Wang. “Torque distribution strategy for a front-and rear-wheel-driven electric vehicle”. In: *IEEE Transactions on Vehicular Technology* 61.8 (2012), pp. 3365–3374.
- [16] Wang Da and Wang Bo. “Research on driving force optimal distribution and fuzzy decision control system for a dual-motor electric vehicle”. In: *2015 34th Chinese Control Conference (CCC)*. IEEE. 2015, pp. 8146–8153.
- [17] Minghui Hu, Jianfeng Zeng, Shaozhi Xu, Chunyun Fu, and Datong Qin. “Efficiency study of a dual-motor coupling EV powertrain”. In: *IEEE Transactions on Vehicular Technology* 64.6 (2014), pp. 2252–2260.
- [18] Pedro Daniel Urbina Coronado, Horacio Ahuett-Garza, et al. “Control strategy for power distribution in dual motor propulsion system for electric vehicles”. In: *Mathematical Problems in Engineering* 2015 (2015).
- [19] Chengning Zhang, Shuo Zhang, Guangwei Han, and Haipeng Liu. “Power management comparison for a dual-motor-propulsion system used in a battery electric bus”. In: *IEEE Transactions on Industrial Electronics* 64.5 (2016), pp. 3873–3882.
- [20] Dongmei Wu, Yang Li, Jianwei Zhang, and Changqing Du. “Torque distribution of a four in-wheel motors electric vehicle based on a PMSM system model”. In: *Proceedings of the Institution of Mechanical Engineers, Part D: Journal of Automobile Engineering* 232.13 (2018), pp. 1828–1845.



- [21] C Chatzikomis, M Zanchetta, P Gruber, A Sorniotti, B Modic, T Motaln, L Blagotinsek, and G Gotovac. “An energy-efficient torque-vectoring algorithm for electric vehicles with multiple motors”. In: *Mechanical systems and signal processing* 128 (2019), pp. 655–673.
- [22] Arash M Dizqah, Basilio Lenzo, Aldo Sorniotti, Patrick Gruber, Saber Fallah, and Jasper De Smet. “A fast and parametric torque distribution strategy for four-wheel-drive energy-efficient electric vehicles”. In: *IEEE Transactions on Industrial Electronics* 63.7 (2016), pp. 4367–4376.
- [23] JW Shin, JO Kim, JY Choi, and SH Oh. “Design of 2-speed transmission for electric commercial vehicle”. In: *International Journal of Automotive Technology* 15 (2014), pp. 145–150.
- [24] Guang Wu, Xing Zhang, and Zuomin Dong. *Impacts of two-speed gearbox on electric vehicle’s fuel economy and performance*. Tech. rep. SAE Technical Paper, 2013.
- [25] Z Zhang, C Zuo, W Hao, Y Zuo, XL Zhao, and M Zhang. “Three-speed transmission system for purely electric vehicles”. In: *International Journal of Automotive Technology* 14 (2013), pp. 773–778.
- [26] Wootae Kim, Daekuk Kim, Dokyeong Lee, Iljoo Moon, and Jinwook Lee. “Analysis of Optimal Shift Pattern Based on Continuously Variable Transmission of Electric Vehicle for Improving Driving Distance”. In: *Applied Sciences* 13.2 (2023), p. 1190.
- [27] EV Data. Electric Vehicle Database. <https://ev-database.org/> (Accessed on 2023-08-25). 2023 – v4.4.
- [28] C Rențea, M Oprean, M Bățăuș, and G Frățilă. “The influence of multi-speed transmissions on electric vehicles energy consumption”. In: *IOP Conference Series: Materials Science and Engineering*. Vol. 564. 1. IOP Publishing. 2019, p. 012107.
- [29] Kihan Kwon, Junhyeong Jo, and Seungjae Min. “Multi-objective gear ratio and shifting pattern optimization of multi-speed transmissions for electric vehicles considering variable transmission efficiency”. In: *Energy* 236 (2021), p. 121419.
- [30] Bo Zhu, Nong Zhang, Paul Walker, Xingxing Zhou, Wenzhang Zhan, Yueyuan Wei, and Nanji Ke. “Gear shift schedule design for multi-speed pure electric vehicles”. In: *Proceedings of the Institution of Mechanical Engineers, Part D: Journal of Automobile Engineering* 229.1 (2015), pp. 70–82.
- [31] Gui-Bin Sun, Yi-Jui Chiu, Wen-Yang Zuo, Shen Zhou, Jian-Chao Gan, and Ying Li. “Transmission ratio optimization of two-speed gearbox in battery electric passenger vehicles”. In: *Advances in Mechanical Engineering* 13.6 (2021), p. 16878140211022869.
- [32] Jiageng Ruan and Qiang Song. “A novel dual-motor two-speed direct drive battery electric vehicle drivetrain”. In: *IEEE Access* 7 (2019), pp. 54330–54342.

- [33] Junnian Wang, Chunlin Zhang, Dachang Guo, Fang Yang, Zhenhao Zhang, and Mengyuan Zhao. “Drive-cycle Based Configuration Design and Energy Efficiency Analysis of Dual-Motor 4WD System with Two-speed Transmission for Electric Vehicles”. In: *IEEE Transactions on Transportation Electrification* (2023).
- [34] Infineon Technologies. *Silicon Carbide CoolSiC™ MOSFETs*. 2023. URL: <https://www.infineon.com/cms/en/product/power/mosfet/silicon-carbide/>.
- [35] GROB-WERKE GmbH Co. KG. *Electric Motors and e-Machines*. 2023. URL: <https://www.grobgroup.com/en/products/product-range/electromobility/e-motor/>.
- [36] Nancy McGuire. “The brave new world of electric vehicle fluids”. In: *Tribology & Lubrication Technology* 77.10 (2021), pp. 30–38.
- [37] Monica Tutuiianu, Pierre Bonnel, Biagio Ciuffo, Takahiro Haniu, Noriyuki Ichikawa, Alessandro Marotta, Jelica Pavlovic, and Heinz Steven. “Development of the World-wide harmonized Light duty Test Cycle (WLTC) and a possible pathway for its introduction in the European legislation”. In: *Transportation research part D: transport and environment* 40 (2015), pp. 61–75.
- [38] Peter Mock, John German, Anup Bandivadekar, and Iddo Riemersma. “Discrepancies between type-approval and “real-world” fuel-consumption and CO”. In: *The International Council on Clean Transportation* 13 (2012).
- [39] Rui Ma, Elena Breaz, and Fei Gao. “Power demand for fuel cell system in hybrid vehicles”. In: *Fuel Cells for Transportation*. Elsevier, 2023, pp. 279–303.
- [40] Keith B Wipke, Matthew R Cuddy, and Steven D Burch. “ADVISOR 2.1: A user-friendly advanced powertrain simulation using a combined backward/forward approach”. In: *IEEE transactions on vehicular technology* 48.6 (1999), pp. 1751–1761.
- [41] Federico Millo, Luciano Rolando, and Maurizio Andreatta. “Numerical simulation for vehicle powertrain development”. In: *Numerical Analysis-Theory and Application*. IntechOpen, 2011.
- [42] Ganesh Mohan, Francis Assadian, and Stefano Longo. “Comparative analysis of forward-facing models vs backwardfacing models in powertrain component sizing”. In: *IET hybrid and electric vehicles conference 2013 (HEVC 2013)*. IET. 2013, pp. 1–6.
- [43] T Holdstock, A Sorniotti, M Everitt, M Fracchia, S Bologna, and S Bertolotto. “Energy consumption analysis of a novel four-speed dual motor drivetrain for electric vehicles”. In: *2012 IEEE vehicle power and propulsion conference*. IEEE. 2012, pp. 295–300.
- [44] Minghui Hu, Shuang Chen, and Jianfeng Zeng. “Control strategy for the mode switch of a novel dual-motor coupling powertrain”. In: *IEEE Transactions on Vehicular Technology* 67.3 (2017), pp. 2001–2013.

- [45] Jianjun Hu, Lingling Zheng, Meixia Jia, Yi Zhang, and Tao Pang. “Optimization and model validation of operation control strategies for a novel dual-motor coupling-propulsion pure electric vehicle”. In: *Energies* 11.4 (2018), p. 754.
- [46] Shuo Zhang, Chengning Zhang, Guangwei Han, Qinghui Wang, et al. “Optimal control strategy design based on dynamic programming for a dual-motor coupling-propulsion system”. In: *The Scientific World Journal* 2014 (2014).
- [47] Olle Sundstrom and Lino Guzzella. “A generic dynamic programming Matlab function”. In: *2009 IEEE control applications, (CCA) & intelligent control, (ISIC)*. IEEE. 2009, pp. 1625–1630.
- [48] Richard Bellman. “Dynamic programming”. In: *Science* 153.3731 (1966), pp. 34–37.
- [49] Lino Guzzella, Antonio Sciarretta, et al. *Vehicle propulsion systems*. Vol. 1. Springer, 2007.
- [50] Xin Lai, Shuyu Wang, Shangde Ma, Jingying Xie, and Yuejiu Zheng. “Parameter sensitivity analysis and simplification of equivalent circuit model for the state of charge of lithium-ion batteries”. In: *Electrochimica Acta* 330 (2020), p. 135239.
- [51] Julian Estaller, Anton Kersten, Manuel Kuder, Ali Mashayekh, Johannes Buberger, Torbjörn Thiringer, Richard Eckerle, and Thomas Weyh. “Battery Impedance Modeling and Comprehensive Comparisons of State-Of-The-Art Cylindrical 18650 Battery Cells considering Cells’ Price, Impedance, Specific Energy and C-Rate”. In: *2021 IEEE International Conference on Environment and Electrical Engineering and 2021 IEEE Industrial and Commercial Power Systems Europe (EEEIC / I&CPS Europe)*. 2021, pp. 1–8. DOI: 10.1109/EEEIC/ICPSEurope51590.2021.9584562.
- [52] Julian Estaller, Anton Kersten, Manuel Kuder, Torbjörn Thiringer, Richard Eckerle, and Thomas Weyh. “Overview of Battery Impedance Modeling Including Detailed State-of-the-Art Cylindrical 18650 Lithium-Ion Battery Cell Comparisons”. In: *Energies* 15.10 (2022), p. 3822.
- [53] XD Xue, Ka Wai Eric Cheng, and NC Cheung. “Selection of electric motor drives for electric vehicles”. In: *2008 Australasian Universities power engineering conference*. IEEE. 2008, pp. 1–6.
- [54] Nasser Hashemnia and Behzad Asaei. “Comparative study of using different electric motors in the electric vehicles”. In: *2008 18th international conference on electrical machines*. IEEE. 2008, pp. 1–5.
- [55] Wei Tong. *Mechanical design of electric motors*. CRC press, 2014.
- [56] Ahmed Al-Timimy, Paolo Giangrande, Michele Degano, Michael Galea, and Chris Gerada. “Investigation of ac copper and iron losses in high-speed high-power density PMSM”. In: *2018 XIII International Conference on Electrical Machines (ICEM)*. IEEE. 2018, pp. 263–269.

- [57] Power Semiconductors. “Application manual power semiconductors”. In: *SEMIKRON International GmbH: Nuremberg, Germany* (2010).
- [58] Kichiro Yamamoto, Katsuji Shinohara, and Hitoshi Makishima. “Comparison between flux weakening and PWM inverter with voltage booster for permanent magnet synchronous motor drive”. In: *Proceedings of the Power Conversion Conference-Osaka 2002 (Cat. No. 02TH8579)*. Vol. 1. IEEE. 2002, pp. 161–166.
- [59] Kichiro Yamamoto, Katsuji Shinohara, and Takahiro Nagahama. “Characteristics of permanent-magnet synchronous motor driven by PWM inverter with voltage booster”. In: *IEEE Transactions on Industry Applications* 40.4 (2004), pp. 1145–1152.
- [60] Jorge O Estima and Antonio J Marques Cardoso. “Efficiency analysis of drive train topologies applied to electric/hybrid vehicles”. In: *IEEE Transactions on Vehicular Technology* 61.3 (2012), pp. 1021–1031.
- [61] Michael H Bierhoff and Friedrich W Fuchs. “Semiconductor losses in voltage source and current source IGBT converters based on analytical derivation”. In: *2004 IEEE 35th Annual Power Electronics Specialists Conference (IEEE Cat. No. 04CH37551)*. Vol. 4. IEEE. 2004, pp. 2836–2842.
- [62] Yuan Zhu, Mingkan Xiao, Xiezu Su, Gang Yang, Ke Lu, and Zhihong Wu. “Modeling of conduction and switching losses for IGBT and FWD based on SVPWM in automobile electric drives”. In: *Applied Sciences* 10.13 (2020), p. 4539.
- [63] Alessandro Acquaviva, Artem Rodionov, Anton Kersten, Torbjörn Thiringer, and Yujing Liu. “Analytical conduction loss calculation of a mosfet three-phase inverter accounting for the reverse conduction and the blanking time”. In: *IEEE Transactions on Industrial Electronics* 68.8 (2020), pp. 6682–6691.
- [64] Sepideh Amirpour, Torbjörn Thiringer, and Dan Hagstedt. “Energy Loss Analysis in a SiC/IGBT Propulsion Inverter over Drive Cycles Considering Blanking time, MOSFET’s Reverse Conduction and the Effect of Thermal Feedback”. In: *2020 IEEE Energy Conversion Congress and Exposition (ECCE)*. IEEE. 2020, pp. 1505–1511.
- [65] Dong Jiang, Rolando Burgos, Fei Wang, and Dushan Boroyevich. “Temperature-dependent characteristics of SiC devices: Performance evaluation and loss calculation”. In: *IEEE Transactions on Power Electronics* 27.2 (2011), pp. 1013–1024.
- [66] Peter Gustavsson Mårdestam and Adam Lundin. *Efficiency Analysis of a Planetary Gearbox*. 2010.
- [67] Vasilios Bakolas, Philipp Roedel, Oliver Koch, and Michael Pausch. “A first approximation of the global energy consumption of ball bearings”. In: *Tribology Transactions* 64.5 (2021), pp. 883–890.

- [68] S Laruelle, C Fossier, C Changenet, F Ville, and S Koechlin. “Experimental investigations and analysis on churning losses of splash lubricated spiral bevel gears”. In: *Mechanics & Industry* 18.4 (2017), p. 412.
- [69] S Seetharaman and A Kahraman. “Load-independent spin power losses of a spur gear pair: model formulation”. In: (2009).
- [70] Jiageng Ruan, Paul Walker, and Nong Zhang. “A comparative study energy consumption and costs of battery electric vehicle transmissions”. In: *Applied energy* 165 (2016), pp. 119–134.
- [71] Frans JR Verbruggen, Varun Rangarajan, and Theo Hofman. “Powertrain design optimization for a battery electric heavy-duty truck”. In: *2019 American Control Conference (ACC)*. IEEE. 2019, pp. 1488–1493.
- [72] Michael A Roscher, Roland Michel, and Wolfgang Leidholdt. “Improving energy conversion efficiency by means of power splitting in dual drive train EV applications”. In: *International Journal of Vehicular Technology* 2013 (2013).
- [73] Wang Da and Wang Bo. “Research on driving force optimal distribution and fuzzy decision control system for a dual-motor electric vehicle”. In: *2015 34th Chinese Control Conference (CCC)*. IEEE. 2015, pp. 8146–8153.
- [74] Nobuyoshi Mutoh. “Front-and-rear-wheel-independent-drive-type electric vehicle (FRID EV) with compatible driving performance and safety”. In: *World Electric Vehicle Journal* 3.1 (2009), pp. 17–26.
- [75] Marco Veliz Castro, Shruthi Mukundan, Claudio Lopes Filho, Glenn Byczynski, Bruce Minaker, Jimi Tjong, and Narayan C. Kar. “A Review of Existing Multi-Motor Electric Powertrain Sizing Strategies”. In: *2021 24th International Conference on Electrical Machines and Systems (ICEMS)*. 2021, pp. 2419–2424. DOI: 10.23919/ICEMS52562.2021.9634221.
- [76] Nobuyoshi Mutoh, Takuro Kazama, and Kazuya Takita. “Driving characteristics of an electric vehicle system with independently driven front and rear wheels”. In: *IEEE Transactions on Industrial Electronics* 53.3 (2006), pp. 803–813.
- [77] Utkal Ranjan Muduli, Abdul R. Beig, Khaled Al Jaafari, Jamal Y. Alsawalhi, and Ranjan Kumar Behera. “Interrupt-Free Operation of Dual-Motor Four-Wheel Drive Electric Vehicle Under Inverter Failure”. In: *IEEE Transactions on Transportation Electrification* 7.1 (2021), pp. 329–338. DOI: 10.1109/TTE.2020.2997354.
- [78] Uwe Vollmer and Uwe Schäfer. “An at-all operating points highly efficient PMSM for HEV”. In: *World Electric Vehicle Journal* 2.4 (2008), pp. 334–342.
- [79] EV reviews. EV tech specs. <https://www.myeveview.com> (Accessed on 2023-02-03). 2023.

- [80] Lino Di Leonardo, Giuseppe Fabri, Andrea Credo, Marco Tursini, and Marco Villani. “Impact of Wire Selection on the Performance of an Induction Motor for Automotive Applications”. In: *Energies* 15.11 (2022), p. 3876.
- [81] Shaohua Sun, Maosen Gong, Baogui Wu, and Yupeng Zou. “Research on optimal meshing speed difference based on shift success probability for dog Clutch in automated manual transmission”. In: *IOP Conference Series: Materials Science and Engineering*. Vol. 892. 1. IOP Publishing. 2020, p. 012052.
- [82] Gergely Bóka, János Márialigeti, László Lovas, and Balázs Trencsényi. “Face dog clutch engagement at low mismatch speed”. In: *Periodica Polytechnica Transportation Engineering* 38.1 (2010), pp. 29–35.
- [83] Cong Guo, Chunyun Fu, Ronghua Luo, and Guanlong Yang. “Energy-oriented car-following control for a front-and rear-independent-drive electric vehicle platoon”. In: *Energy* 257 (2022), p. 124732.
- [84] Huseyin Ayhan Yavasoglu, Junyi Shen, Chuan Shi, Metin Gokasan, and Alireza Khaligh. “Power Split Control Strategy for an EV Powertrain With Two Propulsion Machines”. In: *IEEE Transactions on Transportation Electrification* 1.4 (2015), pp. 382–390. DOI: 10.1109/TTE.2015.2504406.
- [85] Nan Zhao, Nigel Schofield, Rong Yang, and Ran Gu. “Investigation of DC-link voltage and temperature variations on EV traction system design”. In: *IEEE Transactions on Industry Applications* 53.4 (2017), pp. 3707–3718.
- [86] Shan Yin, King Jet Tseng, Rejeki Simanjorang, and Pengfei Tu. “Experimental comparison of high-speed gate driver design for 1.2-kV/120-A Si IGBT and SiC MOSFET modules”. In: *IET Power Electronics* 10.9 (2017), pp. 979–986.
- [87] Anton Kersten, Karl Oberdieck, Andreas Bubert, Markus Neubert, Emma Arfa Grunditz, Torbjörn Thiringer, and Rik W De Doncker. “Fault detection and localization for limp home functionality of three-level NPC inverters with connected neutral point for electric vehicles”. In: *IEEE Transactions on Transportation Electrification* 5.2 (2019), pp. 416–432.
- [88] Wolfgang Wenzel, Prashant Hegde, and Gabriel Domingues. “Optimized System Voltage Level for Increased Efficiency of Battery-electric Vehicles”. In: *ATZextra worldwide* 28.1 (2023), pp. 18–21.
- [89] Davide Cittanti, Enrico Vico, and Iustin Radu Bojoi. “New FOM-based performance evaluation of 600/650 V SiC and GaN semiconductors for next-generation EV drives”. In: *IEEE Access* 10 (2022), pp. 51693–51707.

Table 6.1: Coefficients of polynomial equations for solving battery current.

Transistor	Operation	a	b	c	d
IGBT	Propulsion	$I_{\text{ref}} \cdot R_i \cdot r_d - I_{\text{ref}} \cdot R_i \cdot r_{ce}$	$I_{\text{ref}} \cdot V_{oc} \cdot r_{ce} + I_{\text{ref}} \cdot R_i \cdot V_{d0} - I_{\text{ref}} \cdot V_{oc} \cdot r_d - I_{\text{ref}} \cdot V_{dc} \cdot r_{ce} - I_{\text{ref}} \cdot R_i \cdot V_{dc} - I_{\text{ref}} \cdot R_i \cdot V_{ce0}$	$I_{\text{ref}} \cdot V_{dc} \cdot V_{oc} + I_{\text{ref}} \cdot V_{ce0} \cdot V_{oc} - E_{\text{sw}} \cdot V_{dc} \cdot f_{\text{sw}} \cdot \left( \frac{V_{dc}}{U_{\text{ref}}} \right) - E_{\text{rec}} \cdot V_{dc} \cdot f_{\text{sw}} \cdot \left( \frac{V_{dc}}{U_{\text{ref}}} \right)^{0.6} - I_{\text{ref}} \cdot V_{d0} \cdot V_{oc} - I_{\text{ref}} \cdot V_{ce0} \cdot V_{dc}$	$-I_{\text{ref}} \cdot P_{dc} \cdot V_{dc}$
	Regeneration	$I_{\text{ref}} \cdot R_i \cdot r_{ce} - I_{\text{ref}} \cdot R_i \cdot r_d$	$I_{\text{ref}} \cdot V_{oc} \cdot r_d + I_{\text{ref}} \cdot R_i \cdot V_d - I_{\text{ref}} \cdot V_{dc} \cdot r_d - I_{\text{ref}} \cdot V_{oc} \cdot r_{ce} - I_{\text{ref}} \cdot R_i \cdot V_{dc} - I_{\text{ref}} \cdot R_i \cdot V_{ce0}$	$E_{\text{sw}} \cdot V_{dc} \cdot f_{\text{sw}} \cdot \left( \frac{V_{dc}}{U_{\text{ref}}} \right)^{1.3} + E_{\text{rec}} \cdot V_{dc} \cdot f_{\text{sw}} \cdot \left( \frac{V_{dc}}{U_{\text{ref}}} \right)^{0.6} + I_{\text{ref}} \cdot V_{d0} \cdot V_{dc} + I_{\text{ref}} \cdot V_{oc} \cdot V_{dc} + I_{\text{ref}} \cdot V_{oc} \cdot V_{ce0} - I_{\text{ref}} \cdot V_{oc} \cdot V_{d0}$	$-I_{\text{ref}} \cdot P_{dc} \cdot V_{dc}$
MOSFET	Propulsion	-	$r_{ds}$	$2 \cdot \frac{E_{\text{sw}} \cdot f_{\text{sw}}}{I_{\text{ref}}} \cdot \left( \frac{V_{dc}}{U_{\text{ref}}} \right)^{1.4}$	$P_{dc} - V_{oc} \cdot R_i$
	Regeneration	-	$r_{ds} + R_i$	$-V_{oc} - 2 \cdot \frac{E_{\text{sw}} \cdot f_{\text{sw}}}{I_{\text{ref}}} \cdot \left( \frac{V_{dc}}{U_{\text{ref}}} \right)^{1.4}$	$P_{dc}$